Review

The Influence of Photoactive Heterostructures on the Photocatalytic Removal of Dyes and Pharmaceutical Active Compounds: A Mini-Review

Alexandru Enesca * and Luminita Andronic

Product Design, Mechatronics and Environmental Department, Transilvania University of Brasov, Eroilor 29 Street, 35000 Brasov, Romania; andronic-luminita@unitbv.ro
* Correspondence: aenesca@unitbv.ro; Tel.: +40-732-71-2472

check for updates

Abstract: The diversification of pollutants type and concentration in Wastewater has underlined the importance of finding new alternatives to traditional treatment methods. Advanced oxidation processes (AOPs), among others, are considered as promising candidate to efficiently remove organic pollutants such as dyes or pharmaceutical active compounds (PhACs). The present minireview resumes several recent achievements on the implementation and optimization of photoactive heterostructures used as photocatalysts for dyes and PhACs removal. The paper is focused on various methods of enhancing the heterostructure photocatalytic properties by optimizing parameters such as synthesis methods, composition, crystallinity, morphology, pollutant concentration and light irradiation.

Keywords: semiconductors; heterostructures; photocatalysis; dyes; pharmaceutical compounds

1. Introduction

The increase of the World population, especially in the last 50 years has stimulated the industrial growth and Water consumption. However, With the rapid development of industrialization, the presence of organic pollutants in Water and environment is now an important problem, creating hazardous threats to the ecological system [1–3].

Dyes and pharmaceutical compounds represent two important classes of organic pollutants affecting the Water and human life quality [4,5]. The contamination With dyes substances such as rhodamine B (RhB), malachite green (MG), methyl orange (MO), etc. have raised serious issues related to human health. Most of the dyes are considered harmful due to the high toxicity and carcinogenicity induced by their nonbiodegradable aromatic structure [6–8]. Pharmaceutically active compounds (PhACs), such as tetracycline (TC), ciprofloxacin (CIP), triclosan (TCS), carbamazepine (CBZ), salicylic acid (SA), ibuprofen (IBS) and sulfamethazine (SMZ), etc., are helpful to cure human diseases but the pollution from metabolized or partially metabolized pharmaceutical Wastes is already recognized as a hazard [9–11].

Advanced oxidation processes (AOPs) represent an energy-efficient and green approach suitable for environmental remediation, particularly optimized for Wastewater treatment due to the use of solar energy as a driving force to initiate the oxidation reactions [12–14]. The photocatalysis is considered as an advanced oxidation process, using stand-alone or coupled semiconductors as Well as other composite materials [15–17].

Breakthrough heterostructures that benefit from the full range of solar light have attracted the attention of many scientists, the UV, visible or near infrared photoexcitation depending on their band gaps energy and ability to generate (super)oxidative species able to destroy organic pollutants [18,19].

Owing to the controllable band structures and efficient electron-hole separation, the heterostructured photocatalyst exhibits a superior performance to their individual components [20–22].

The synergistic effect of coupling photocatalysis With other techniques in order to improve the pollutant degradation efficiency Was studied by many research groups. Coupling adsorption With photocatalysis has shown promising results on RhB [23] and MG [24] dyes removal. Encouraging results Were obtained on PhACs [25,26] and dyes [27] removal by coupling biodegradation With photocatalysis. Enhanced mineralization conversion efficiencies Were obtained by coupling flocculation With photocatalysis [28], ultrasound With photocatalysis [29] and plasma With photocatalysis [30].

The present minireview resumes several recent achievements on the implementation and optimization of photoactive heterostructures used as photocatalysts for dyes and PhACs removal. Many other papers Which are not included here have the potential to contain highly innovative Work. The paper is focused on the influence of crystallinity, morphology, pollutant concentration, irradiation time and light spectra on the photocatalytic activity of various heterostructures. This minireview make a comparative evaluation of the radiation intensity and spectra required for organic pollutant removal based on the heterostructure charge transport mechanism. The photocatalytic efficiency refers to partial or total pollutant degradation according to the information's provided in the literature. The lack of standardization regarding the photocatalysis experimental parameters has, as a consequence, the presence of various scientific papers containing data difficult to compare.

2. Heterostructure Mechanisms for Photocatalytic Application

Photocatalysis is a chemical process mediated by one or more semiconductors, Which under irradiation increase the reduction and oxidation (redox) reactions rate based on charge carriers' generation [31,32]. When the chemical potential of the electrons from the conduction-band (CB) is between +0.5 and −2.0 V versus the normal hydrogen electrode (NHE), they act as reductants due to the strong oxidizability [33–35]. The photocatalytic process is characterized by three main steps: (i) electron-hole pair's generation due to the light absorption, (ii) the diffusion of photoexcited charge carriers on the semiconductor surface and (iii) the redox reaction on the semiconductor surface [36–38].

As presented in Figure 1, during the photocatalytic degradation of organic pollutants, the photogenerated electrons and holes are trapped by dissolved O_2 and H_2O [39,40]. Highly reactive oxygen species, including superoxide (O_2^-) and hydroxyl radicals (OH), are developed under light irradiation [41,42]. If the organic pollutants contain only carbon, oxygen and hydrogen atoms, it can be degraded to by-products or even completely mineralized (CO_2 and H_2O). However, the major part of dyes and PhACs contains also other atoms, and the mineralization occurs With the formation of additional products (based on Cl^-, NH_4^+, SO_3^{2-}, etc.) [43,44].
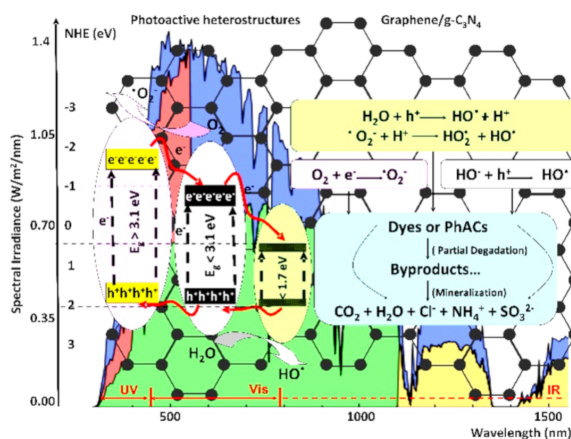

Figure 1. Photoactive heterostructures and the corresponding photocatalytic reactions.

Photoactive heterostructures are considered as composite materials developed by using at least two components/compounds With similar or different chemical nature and able to develop charge carriers during the light irradiation [45–47]. The literature outlines four typical heterostructures mechanisms (p-n junctions, type II heterostructures, Schottky junctions and Z-scheme heterostructures) mostly used in photocatalytic studies.

The p-n junctions (see Figure 2) mimics the photovoltaic cell mechanism but With the difference that the charge carriers are used in redox reactions. Between the p-type and n-type semiconductors, an interfacial region is formed and the electrons from the CB of the p-type semiconductor migrate to the n-type semiconductor. The holes follow the reverse direction, from the n-type semiconductor VB to the p-type semiconductor VB forming a space-charge region. Due to the charge carrier's diffusion, the space-charge region Will have an established built-in potential directing the electrons and holes flow in opposite directions [48–50].
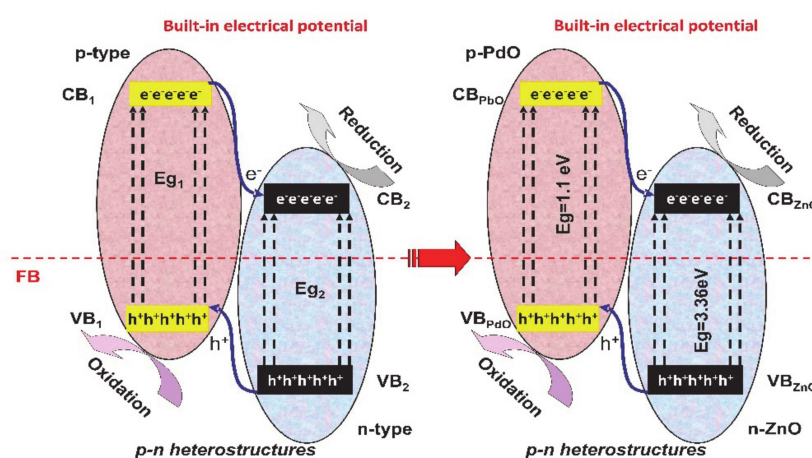

Figure 2. The p-n junction's mechanism.

In the type-II (see Figure 3), the potential difference between the semiconductors Will easily separate electrons and holes, preventing subsequent carrier recombination. The reason consists on the fact that the CB and VB of one semiconductor are higher than that of the other semiconductor, Which assures an effective separation With holes and electrons at different sides of the heterojunction [51–53].
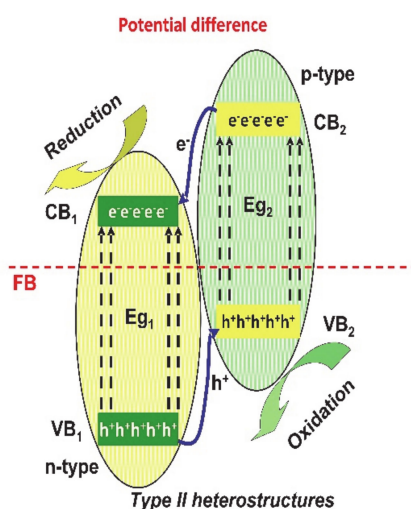

Figure 3. The type-II heterostructures mechanism.

The Schottky junctions (see Figure 4) represented by the semiconductor–metal interface, can induce an effective Way to reduce charge carriers' recombination and extend the spectral light absorption of the semiconductor. One of the most important features is represented by the localized surface plasmonic resonance (LSPR) effect, Which assures the visible light absorption and the excitation of active electrons/holes pairs. The LSPR takes place When the Work function of the metal surpasses that of the semiconductor, developing a positive space-charge region on the semiconductor surface as Well as an upwards of the semiconductor band [54–56].
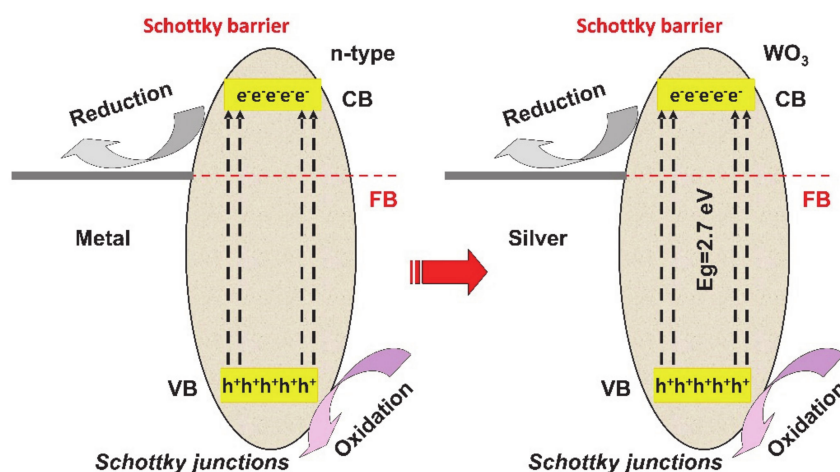
Figure 4. Schottky junction's mechanism.

The Z-scheme (see Figure 5) consists of two connected photocatalytic systems, With the advantage of endowing charge carriers With stronger reduction/oxidation properties.
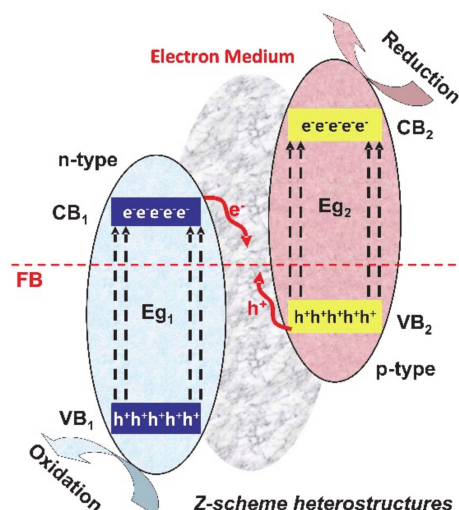
Figure 5. Z-scheme heterostructures for photocatalytic applications.

These systems can use shuttle redox mediators, solid-state electron mediators or no electron mediators. The photogenerated electrons from the second photocatalytic systems Will migrate to the electron medium, in order to recombine With the photogenerated holes from the first photocatalytic system. In this Way, the opposite electrons and holes are involved in the reduction and oxidation reactions, Which assure a highly efficient charge separation [57–59].

A relatively new type of heterostructure mechanism is represented by S-scheme (see Figure 6), Where the photogenerated electrons from photocatalyst I With lower conduction band (CB) potential Will combine the photogenerated holes from photocatalyst II With higher valence band (VB) potential based on the driving force of the internal electric field, thereby inducing the spatial separation of charge carriers under irradiation, considering the conditions of ensuring the strong redox ability [60].
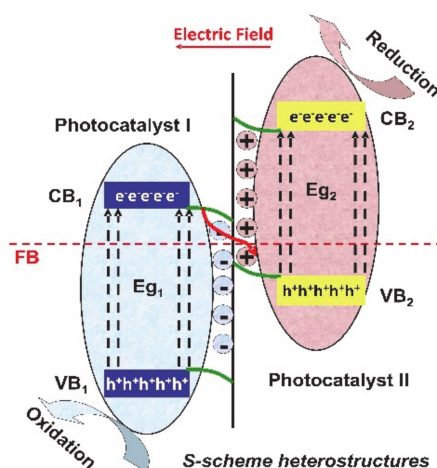

Figure 6. The mechanism of S-scheme heterostructures.

3. Photocatalytic Organic Pollutants Removal by Heterostructures

3.1. Dyes

Dyes are substances With complex chemical structures involving aromatic cycles and functional groups [61–63]. There are several classifications such as acid dyes, alkaline dyes, azo dyes, sulphur dye, etc., most of them considering the composition and the solubility in Water. Between others, the literature mentions the following representative dyes: RhB, methylene blue (MB), MO and MG. These dyes molecules are characterized by aromatic structures With high chemical stability toward traditional Wastewater treatment processes. Table 1 includes representative studies regarding photocatalysts materials (composition, synthesis method, morphology and crystallinity) and photocatalytic parameters (pollutant concentration, radiation type, intensity and time), influencing the dyes photocatalytic removal process (efficiency and rate constant).

The RhB photocatalytic removal using g-C_3N_4-based heterostructures obtained by ultrasonication [64,65] and hydrothermal [66,67] methods Were investigated in the presence of Vis irradiation. The $Bi_{12}TiO_{20}$/g-C_3N_4 [64] and $Bi_{3.84}W_{0.16}O_{6.24}$ (BWO)/g-C_3N_4 [65] heterostructures Were evaluated in similar photocatalytic conditions (10 mg/L RhB and 50 min irradiation period), but With different light intensities (500 W for $Bi_{12}TiO_{20}$/g-C_3N_4 and 100 W for $Bi_{3.84}W_{0.16}O_{6.24}$ (BWO)/g-C_3N_4). Using smaller radiation intensity, the $Bi_{3.84}W_{0.16}O_{6.24}$ (BWO)/g-C_3N_4 heterostructure exhibits higher photocatalytic efficiency (99.8%) With lower energy consumption than that of $Bi_{12}TiO_{20}$/g-C_3N_4 (97%). Both heterostructures follow the Z-scheme mechanism and have similar crystalline structures, but different morphologies (sheet-like for $Bi_{3.84}W_{0.16}O_{6.24}$ (BWO)/g-C_3N_4 and multilayer for $Bi_{12}TiO_{20}$/g-C_3N_4). A similar observation is valid for TiO_2/g-C_3N_4 [66] and g-C_3N_4/ZnO [67] obtained by the hydrothermal method. In this case, the g-C_3N_4/ZnO heterostructure achieves 98.5% photocatalytic efficiency toward RhB after 70 min of 300 W Vis light irradiation. The TiO_2/g-C_3N_4 reaches only 85% after 100 min of Vis light irradiation (500 W). The g-C_3N_4/ZnO benefit from the large rods shape interfaces, Which improve the energy conversion due to the larger active surface. In TiO_2/g-C_3N_4, there Was tensile stress induced by TiO_2 and compressive stress from C_3N_4, With detrimental influence on the heterostructure interfacial area. However, using the

same irradiation scenario (Vis, 500 W for 100 min) but employing $WS_2/BiOBr$ heterostructure [68], the photocatalytic efficiency of RhB (20 mg/L) has increased up to 95%, due to high Vis absorbance attributed to both partners. Even if the photocatalytic efficiency is lower compared With $g-C_3N_4/ZnO$, the RhB concentration Was double.

Solvothermal method Was used to develop NiO/BiOI S-scheme heterostructure [60], $Bi_2MoO_6/Bi_5O_7Br/TiO_2$ Z-scheme heterostructure [69] and Bi_2MoO_6/Fe_3O [70] type II heterostructure. The optimum energy consumption corresponds to NiO/BiOI reaching 90% RhB (5 mg/L) photocatalytic efficiency in 60 min of irradiation With 300 W Vis light source. The NiO/BiOI is characterized by porous morphology and follows the S-scheme mechanism, in Which the electrons from CB of BiOI migrate towards NiO in the junction interface due to the formation of an internal electric field. The Bi_2MoO_6/Fe_3O heterostructure has higher photocatalytic efficiency (99.5%) but after a longer irradiation period (120 min) With 350 W Vis light source. However, in this case, the RhB concentration Was 20 mg/L, Which means that even if the energy consumption Was higher, the quantity of pollutant removed from the aqueous solution Was also bigger. The Bi_2MoO_6/Fe_3O is a type II heterostructure With flower-like morphology, Who benefit from the surface oxygen vacancies, Which serve as electron-trapping sites, and have an important role in the charge transmission through the heterostructures by facilitating the migration of the bulk electron-hole. Higher energy consumption corresponds to $Bi_2MoO_6/Bi_5O_7Br/TiO_2$, Which follows a Z-scheme mechanism and exhibits 73.43% photocatalytic efficiency of RhB (10 mg/L) after 180 min of irradiation With 500 W Vis light source.

Bi_2MoO_6/Fe_3O type II heterostructure [70] Was employed to investigate MB removal in the same photocatalytic conditions as RhB removal. However, in the case of MB, the photocatalytic efficiency has increased up to 93.81%, indicating that this heterostructure can be optimized for a particular type of pollutant molecule. $Ta_3B_2@Ta_2O_5$ [71] heterostructure Was obtained by in situ growth method, and the photocatalytic properties Were tested in the same conditions as Bi_2MoO_6/Fe_3O (180 min irradiation period, 500 W Vis light source). The photocatalytic efficiency Was lower (80%) compared With Bi_2MoO_6/Fe_3O, but the quantity of RhB removal Was higher, considering that the initial dye concentration Was 5 times bigger (50 mg/L). Concluding, for the same amount of energy consumption the quantity of pollutant removal is significantly higher. The $Ta_3B_2@Ta_2O_5$ heterostructure is characterized by irregular shape particles and contains high crystalline Ta_3B_2 and Ta_2O_5. The heterostructure mechanism corresponds to Schottky junction and has the advantage of the metallic transition zone, Which improves the visible light absorption and the electron collector facilitating the charge transfer from CB of Ta_2O_5 to surface.

The $g-C_3N_4/ZnO$ heterostructure [67] previously presented for RhB removal Was also tested for MB (10 mg/L) removal in the same photocatalytic conditions (70 min, 300 W Vis light source). In this particular study, there Was no significant difference regarding the photocatalytic efficiency values for both dyes (98% MB and 98.5% RhB) meaning that the heterostructure can efficiently remove different organic dye molecules. A similar experiment Was done With $BiPO_{4-x}/B_2S_3$ [72] using half of the MB concentration (5 mg/L) and 300 W Vis light intensity. The photocatalytic efficiency has reached 98% after 360 min of irradiation, Which represents 5 times more energy consumption for a lower pollutant concentration. The $BiPO_{4-x}/B_2S_3$ has a sheets morphology containing monoclinic $BiPO_4$ and orthorhombic Bi_2S_3 and follows a Z-scheme pathway. The lower photocatalytic efficiency can be a consequence of ultraviolet light heterostructure exposure before the photocatalytic experiment, inducing electrons migration during the conversion of oxygen atoms in oxygen vacancy Who may act as the recombination centre of photoinduced charge carriers.

UV light Was used to evaluate the photocatalytic performance of spherical particles $MnFe_2O_4/rGO$ [73] and flower-like Ag/hybridized $1T-2H MoS_2/TiO_2$ [74] after 60 min of irradiation. Both heterostructures exhibit similar efficiencies (~97%) but at different MB concentrations. The $MnFe_2O_4/rGO$ heterostructure obtained by coprecipitation method requires only 40 W light intensity to remove 97% of MB (10 mg/L) due to the reduced graphene oxide insertion (rGO), Which induces a decrease of $MnFe_2O_4$ crystallite size from 21 to 18 nm and increase the junction interfacial area. The

Ag/hybridized 1T-2H MoS_2/TiO_2 obtained by chemical reduction exhibits a dual Schottky junction and Z-scheme mechanisms, and Was able to remove 96.8% of MB (20 mg/L) using 235 W UV light source. Even if the MB concentration Was double, the energy consumption has increased almost 6 times Which make this system less energy efficient. Another heterostructure obtained by coprecipitation method and tested under UV irradiation using 30 mg/L MB aqueous solution Was $ZnAl_2O_4/Bi_2MoO_6$ [75]. The heterostructure exhibits a sheet-like morphology containing koechlinite Bi_2MoO_6 and gahnite $ZnAl_2O_4$, and follow a type II mechanism in Which the VB potential of Bi_2MoO_6 is higher than that of $ZnAl_2O_4$ favouring the formation of superoxidative species. After 180 min of UV irradiation (100 W), the photocatalytic efficiency Was 86.36%, due to the hinder effect of the $ZnAl_2O_4$ on the Bi_2MoO_6 light absorption through the suspension solution.

A comparative study regarding the influence of light spectra on the photocatalytic efficiency at low MB concentration (1 mg/L) Was done using $CuO–TiO_2$ heterostructure [76], obtained by ultrasonication. The TiO_2 fibres sizes Were in the range of 150–500 nm With CuO particles on the surface. The study indicates that $CuO–TiO_2$ follow a p-n heterostructure mechanism With superior photocatalytic properties during UVc irradiation When the rate constant Was 0.135 min^{-1}, almost ten times higher than that in the presence of Vis irradiation. Consequently, after 45 min of UVc (96 W) irradiation, 99% of MB Was removed and the same value Was obtained by Vis (240 W) irradiation but after 240 min.

The influence of 300 W Vis light source on the MO photocatalytic removal Was tested using $LaNiO_3/TiO_2$ S-scheme [77], $ZnFe_2O_4/SnS_2$ p-n [78] and $WO_3/g-C_3N_4$ Z-scheme [79] heterostructures. $ZnFe_2O_4/SnS_2$ heterostructure obtained by the solvothermal method has the lowest energy consumption being able to remove 99% of MO (50 mg/L) in just 20 min. The $ZnFe_2O_4/SnS_2$ heterostructure exhibits irregular particles shape, and the charges transport mechanism is based on the photogenerated electrons migration into the CB of SnS_2 from the CB of $ZnFe_2O_4$. The electron-hole recombination is avoided, due to the photogenerated holes transit from VB of SnS_2 to VB of $ZnFe_2O_4$. $LaNiO_3/TiO_2$ and $WO_3/g-C_3N_4$ show similar photocatalytic activity toward MO (10 mg/L), reaching 100% photocatalytic efficiency in 150 min ($LaNiO_3/TiO_2$) and 93% in 120 min ($WO_3/g-C_3N_4$). The $LaNiO_3/TiO_2$ heterostructure With irregular particles morphology Was obtained by sol–gel technique and contains anatase/rutile TiO_2 as Well as crystalline $LaNiO_3$, both being able to develop separate electron-hole pairs under irradiation. The charge carrier's concentration increases and induces a certain potential difference able to enhance the photocatalytic activity of the S-scheme. The photocatalytic efficiency decreases at 92% When MO concentration is double (20 mg/L), due to the heterostructure limitation to form enough oxidative and superoxidative species in a short period. The porous morphology and small $g-C_3N_4$ sheet provide larger surface area and homogenous spread active sites, housing the photochemical reactions and facilitating the mass transport through the $WO_3/g-C_3N_4$ heterostructure.

The photocatalytic activity decreases When 90 W UVc light Was used to irradiate $Ag_2Mo_{1-x}W_xO_4$ (Ag_2WO_4/Ag_2MoO_4) [80] rod-shaped heterostructure, obtained by the microwave-assisted hydrothermal method. Even if the MO concentration Was relatively low (5 mg/L), the photocatalytic efficiency after 140 min Was 45% due to the available light spectra. The photocatalytic activity can be increased by using an extended light spectrum, considering that both Ag_2WO_4 and Ag_2MoO_4 have good Vis absorbance.

Highly concentrated MG (50 mg/L) aqueous solution Was used to evaluate the photocatalytic properties of TiO_2/WO_3 [81] and CdS@ZnS@ZnO [82] heterostructures. Under Vis irradiation, the TiO_2/WO_3 hollow sphere heterostructure shows a better energy performance reaching 98% photocatalytic efficiency after 60 min using a 300 W light source. The TiO_2/WO_3 composite can efficiently use the visible light to the electronic structure of composite and the quantum effect arising from small particle size. CdS@ZnS@ZnO spherical shape heterostructure obtained by the hydrothermal method has bigger energy consumption and requires 400 W Vis light source for 180 min to remove 32.5 mg/L (65%) from the 50 mg/L MG initial concentration. However, the situation is drastically changed under UV (125 W) light Where the photocatalytic efficiency increases at 95% only after 30 min of irradiation. The CdS@ZnS@ZnO follows a type II mechanism, Where the VB and CB potential of

ZnO are higher than ZnS allowing the photogenerated holes to be transferred on VB of ZnS. When the CdS Was added, the photogenerated electrons could migrate from the CB of ZnS to the CB of CdS and further transferred on the CB of ZnO. It seems reasonable to consider that UV scenario is more energy efficient, but the sustainability issue must be underlined (the available UV sunlight spectra on the Earth surface is rather limited).

La_2CuO_4-decorated ZnO [83] and $MgFe_2O_4/Bi_2MoO_6$ [84] photocatalytic properties based on Z-scheme mechanism Were tested after 120 min of irradiation. The results show that $MgFe_2O_4/Bi_2MoO_6$ With plate morphology reaches 97% photocatalytic efficiency for MG removal (20 mg/L initial concentration) using a 300 W Vis light source. The La_2CuO_4-decorated ZnO heterostructure obtained by in situ extraction exhibits lower photocatalytic efficiency (91%), but at a higher MG concentration (25 mg/L) and in the presence of 125 W Vis light source. Based on the rate constant provided by the authors, the La_2CuO_4-decorated ZnO have a higher rate constant corresponding to MG removal due to the La_2CuO_4 ability to convert visible light and to reduce oxygen molecules to superoxide radicals.

Table 1. Recent representative studies on heterostructures photocatalytic application for dyes removal.

Heterostructure Composition	Synthesis Method	Morphology/Crystallinity	Pollutant and Concentration (mg/L)	Radiation Type, Intensity (*I*), Irradiation Time (*t*)	Efficiency and Rate Constant (min^{-1})	Ref.
$Bi_{12}TiO_{20}/g$-C_3N_4	Ultrasonication	Multilayer structure/cubic $Bi_{12}TiO_{20}$	RhB = 10 MO = 20	Vis I = 500 W t = 50 min	97% (RhB), 90% (MO)/0.0537 (RhB), 0.0328 (MO)	[64]
$Bi_{3.84}W_{0.16}O_{6.24}$ (BWO)/g-C_3N_4	Ultrasonication	Sheets/cubic BWO	RhB = 10	Vis I = 100 W t = 50 min	99.8%/ 0.0562	[65]
$Bi_2MoO_6/Bi_5O_7Br/TiO_2$	Solvothermal	Tube arrays/anatase TiO_2, orthorhombic Bi_2MoO_6	RhB = 10 MO = 16 MB = 6.5	Vis I = 500 W t = 180 min	73.43% (RhB) 47.77% (MO) 93.81% (MB)/0.00742 (RhB) 0.00354 (MO) 0.00225 (MB)	[69]
Bi_2MoO_6/Fe_3O	Solvothermal	Flower/orthorhombic Bi_2MoO_6	RhB = 20	Vis I = 350 W t = 120 min	99.5%/ 0.0364	[70]
NiO/BiOI	Solvothermal	Foam/crystalline NiO	RhB = 4.8	Vis I = 300 W t = 60 min	90%/ 0.0572	[60]
TiO_2/g-C_3N_4	Hydrothermal	2D sheet/pristine 2D-TiO_2	RhB = 10	Vis I = 500 W t = 60 min	85%/ 0.03	[66]
$WS_2/BiOBr$	Hydrothermal	Plates/tetragonal BiOBr	RhB = 20	Vis I = 500 W t = 100 min	95%/ np *	[68]
g-C_3N_4/ZnO	Hydrothermal	Rod/hexagonal wurtzite ZnO	RhB = 10 MB = 10	Vis I = 300 W t = 70 min	98% (MB), 98.5% (RhB)/ np	[67]
$BiPO_{4-x}/B_2S_3$	Hydrothermal	Sheet/monoclinic $BiPO_4$ and orthorhombic Bi_2S_3	MB = 5	Vis I = 300 W t = 360 min	98%/ 0.0222	[72]
$MnFe_2O_4/rGO$	Coprecipitation	Spherical/cubic $MnFe_2O_4$	MB = 10	UV I = 40 W t = 60 min	97%/ 0.0589	[73]
$ZnAl_2O_4/Bi_2MoO_6$	Coprecipitation	Sheet/koechlinite Bi_2MoO_6 and gahnite $ZnAl_2O_4$	MB = 30	UV I = 100 W t = 180 min	86.36%/ 0.638	[75]
Ag/hybridized 1T-2H MoS_2/TiO_2	Chemical reduction	Flower/anatase TiO_2	MB = 20	UV I = 235 W t = 60 min	96.8%/ 0.0539	[74]

Table 1. *Cont.*

Heterostructure Composition	Synthesis Method	Morphology/Crystallinity	Pollutant and Concentration (mg/L)	Radiation Type, Intensity (*I*), Irradiation Time (*t*)	Efficiency and Rate Constant (min^{-1})	Ref.
$Ta_3B_2@Ta_2O_5$	In situ	Powder/crystalline Ta_3B_2 and Ta_2O_5	MB = 50	Vis I = 500 W t = 180 min	80%/ np	[71]
$CuO–TiO_2$	Ultrasonication	Fiber/anatase TiO_2 and monoclinic CuO	MB = 1	UVc, Vis I_{UVc} = 96 W I_{Vis} = 250 W t_{UVc} = 30 min t_{Vis} = 240 min	99% (UVc) 98% (Vis)/ 0.135 (UVc) 0.015 (Vis)	[76]
$WO_3/g\text{-}C_3N_4$	Polymerization	Sheet/crystalline $WO_3/g\text{-}C_3N_4$	MO = 10	Vis I = 300 W t = 120 min	93%/ 0.0213	[79]
$LaNiO_3/TiO_2$	Sol–gel	Particles/perovskite $LaNiO_3$, anatase and rutile TiO_2	MO = 10 MO = 20	Vis I = 300 W t = 150 min	100% (10 mg/L) 92% (20 mg/L)/ np	[77]
$ZnFe_2O_4/SnS_2$	Solvothermal	Particles/crystalline $ZnFe_2O_4$ and SnS_2	MO = 50	Vis I = 300 W t = 20 min	99%/ 0.214	[78]
$Ag_2Mo_{1-x}W_xO_4$	Microwave-assisted hydrothermal	Rod/cubic Ag_2MoO_4, orthorhombic Ag_2WO_4	MO = 5	UVc I = 90 W t = 140 min	45%/ 0.0058	[80]
TiO_2/WO_3	One pot	Hollow sphere/anatase TiO_2 and monoclinic WO_3	MG = 50	Vis I = 300 W t = 60 min	98%/ 0.0746	[81]
La_2CuO_4-decorated ZnO	In situ extraction	Particles/crystalline ZnO, orthorhombic La_2CuO_4	MG = 25	Vis I = 125 W t = 120 min	91%/ 0.063	[83]
$MgFe_2O_4/Bi_2MoO_6$	Hydrothermal	Plates/crystalline Bi_2MoO_6 and $MgFe_2O_4$	MG = 20	Vis I = 300 W t = 120 min	97%/ 0.0113	[84]
CdS@ZnS@ZnO	Hydrothermal	Spherical/cubic ZnS, hexagonal CdS and ZnO	MG = 50	UV, Vis I_{UV} = 125 W I_{Vis} = 400 W t_{UV} = 30 min t_{Vis} = 180 min	95% (UV) 65% (Vis)/ np	[82]

* not provided.

To sum up, the most energy-efficient photocatalytic systems correspond to type II mechanism heterostructures With energy consumption between 62 (47.5 mg/L MG removal by CdS@ZnS@ZnO) and 300 Wh (49 mg/L MG removal by TiO_2/WO_3). Higher energy consumption is attributed to Z-scheme heterostructure ($Bi_2MoO_6/Bi_5O_7Br/TiO_2$), Which uses 1500 Wh to remove 7.3 mg/L of RhB and 7.64 mg/L of MO. However, the correlation between the heterostructure mechanism and the energy consumption must consider other factors as Well (heterostructure composition, pollutant type and concentration, radiation type, etc.).

3.2. Pharmaceutical Active Compounds

The increase of PhACs concentration raises essential issues to traditional Wastewater treatment [85–87] and requires the involvement of novel processes such as photocatalysis [88–90]. The literature mentions a high number of PhACs investigated in AOP experiments, between the most representative are: TC, CIP, TCS, CBZ, SA, IBS and SMZ. Table 2 includes representative studies regarding photocatalysts materials (composition, synthesis method, morphology and crystallinity) and photocatalytic parameters (pollutant concentration, radiation type, intensity and time) influencing the PhACs photocatalytic removal process (efficiency and rate constant).

The photocatalytic removal of TC under Vis light as irradiation source Was evaluated using g-C_3N_4-based heterostructures. Three heterostructures (BN/B-doped-g-C_3N_4 [91], $WO_3/g\text{-}C_3N_4$ [79] and g-C_3N_4-decorated ZrO_{2-x} [92]) following the Z-scheme mechanism Were irradiated With a 300 W Vis light source in order to study the photocatalytic activity toward 10 mg/L TC solution.

g-C$_3$N$_4$-decorated ZrO$_{2-x}$ With tube morphology obtained by anodic oxidation and physical vapour deposition exhibits lower energy consumption, requiring only 60 min to reach 90.6% photocatalytic efficiency. This result Was influenced by the abundant defects states and lattice disorder, allowing ZnO$_{2-x}$ to extend the absorption range to visible spectral region. The interfacial band bending and directed build-in electric field present in the band structure induce an increase of the charge carriers' mobility and concentration. The sheets-like BN/B-doped-g-C$_3$N$_4$ heterostructure obtained by in situ growth exhibits 88.1% photocatalytic efficiency after 60 min of irradiation. The small difference in the photocatalytic efficiency can be induced by the influence of boron doping concentration on the charge carrier mobility. The BN Will canalize the photogenerated charges Without recombination, Which helps electrons to move to the active sites on photocatalyst surface. The boron nitride has a hexagonal structure and does not significantly affect the crystal structure of B-doped-g-C$_3$N$_4$. The highest photocatalytic efficiency (97%) corresponds to WO$_3$/g-C$_3$N$_4$ heterostructure, Who Was presented during MO-dedicated subsection. However, the energy consumption is significantly higher, considering that the irradiation time is three times longer (180 min) just to gain an extra 6.4% at the overall photocatalytic efficiency.

Using a combined type II and Z-scheme mechanisms, the photocatalytic activity of Ag$_3$PO$_4$/Co$_3$(PO$_4$)$_2$/g-C$_3$N$_4$ [93] heterostructure Was tested using a 10 mg/L TC solution. The Ag$_3$PO$_4$/Co$_3$(PO$_4$)$_2$/g-C$_3$N$_4$ heterostructure Was obtained by precipitation method and exhibited flower-like morphology. The photocatalytic efficiency (88%) is similar to BN/B-doped-g-C$_3$N$_4$ (88.1%) but at longer irradiation period (120 min, 300 W Vis light source), Which requires higher energy consumption. The dual electron transfer induced by the combined mechanisms is still a subject of optimization, in order to have a rational design of ternary heterostructure that facilitates multilevel electron transfer.

The TC solution With 20 mg/L concentration Was used to study the photocatalytic activity of two Z-mechanism heterostructures (MoS$_2$/g-C$_3$N$_4$/Bi$_{24}$O$_{31}$Cl$_{10}$ [94] and CuBi$_2$O$_4$/Bi$_2$WO$_6$ [95]), one type II heterostructure (La(OH)$_3$/BiOCl [96]) and one p-n heterostructure (WS$_2$/BiOBr [68]). La(OH)$_3$/BiOCl type II heterostructure With sheets morphology obtained by microwave method shows very low energy consumption and reach 85% photocatalytic efficiency in 60 min of irradiation With a 5 W Vis source. The photocatalytic activity is attributed to the shorted mitigation distance (due to the small BiOCl thickness ~18 nm) followed by the photogenerated electrons during the migration process. The two heterostructures based on Z-mechanism show photocatalytic efficiencies above 90% in the presence of 300 W Vis light source. MoS$_2$/g-C$_3$N$_4$/Bi$_{24}$O$_{31}$Cl$_{10}$ has lower energy consumption and higher photocatalytic efficiency, reaching 97.5% in 60 min While CuBi$_2$O$_4$/Bi$_2$WO$_6$ requires double irradiation period (120 min) to remove 93% of TC. The higher MoS$_2$/g-C$_3$N$_4$/Bi$_{24}$O$_{31}$Cl$_{10}$ photocatalytic efficiency is explained by the ability to Work as a dual Z-scheme ternary heterostructure, in Which each component Will generate charge carriers under irradiation. Consequently, the charge carriers' concentration Will be higher in the ternary heterostructure compared With the binary heterostructure. The p-n heterostructure (WS$_2$/BiOBr) previously described in correlation With RhB dye Was tested for two pharmaceutical molecules, and the photocatalytic efficiency Was 96% for TC and 92% for CIP (20 mg/L). In order to reach these values, the WS$_2$/BiOBr requires 100 min of irradiation using high-intensity (500 W) Vis light source. At the same CIP concentration and irradiation period, the BiOCl/CQDs/rGO [97] sheets-like heterostructure exhibits 87% photocatalytic efficiency using a lower intensity (300 W) Vis light source. Light-harvesting enhancement by CQDs (carbon quantum dots) and rGO (reduced graphene oxide) Was not a crucial factor for increasing the photocatalytic activity, but they have a significant influence on accelerating the charge transfer and suppressing the recombination of photogenerated charge carriers.

An analogue evaluation Was done using two heterostructures (ZnIn$_2$S$_4$/BiPO$_4$ [98] and AgI/Bi$_2$MoO$_6$/AgBi(MoO$_4$)$_2$ [99]) obtained by hydrothermal method and tested using low TC (5 mg/L) and high TC (40 mg/L) concentrations. Both heterostructures Were irradiated With Vis light for 90 min. AgI/Bi$_2$MoO$_6$/AgBi(MoO$_4$)$_2$ With sheets morphology Was tested in 5 mg/L TC solution using a 400 W Vis source, and the photocatalytic efficiency Was 91.9%. Contrary, the ZnIn$_2$S$_4$/BiPO$_4$ With flower-like morphology Was tested at a higher TC concentration (40 mg/L) but using lower Vis light source

intensity (300 W), and the photocatalytic efficiency Was 84%. These results show that by optimizing the heterostructure composition, it is possible to remove higher (eight times) pollutant concentrations With lower energy consumption. $AgI/Bi_2MoO_6/AgBi(MoO_4)_2$ follows a Z-scheme mechanism and has the advantage of ternary structure With multiple charge carriers' injection. $ZnIn_2S_4/BiPO_4$ is a type II heterostructure Who benefit from the high specific surface ($\sim$100 m^2/g) due to the dandelion-like microflower structure.

Z-scheme ($PVPbiochar@ZnF_2O_4/BiOBr$ [100]) and S-scheme ($LaNiO_3/TiO_2$ [77]) mechanisms Were used to evaluate the CIP photocatalytic removal under Vis light (300 W). The $PVPbiochar@ZnF_2O_4/BiOBr$ heterostructure With sheets-like morphology Was obtained by the solvothermal method and contains tetragonal BiOBr and spinel $ZnFe_2O_4$. The Z-scheme heterostructure exhibits 84% photocatalytic efficiency (15 mg/L CIP concentration and 60 min irradiation period). Biochar and graphene have similar electrical properties, and the photogenerated holes are trapped by BiOBr reacting directly With CIP or H_2O to form HO^- species. $LaNiO_3/TiO_2$ heterostructure has a granular morphology and Was obtained by in situ sol–gel process. The S-scheme requires 180 min of irradiation in order to achieve 55% photocatalytic efficiency in a less concentrated CIP solution (10 mg/L). The higher energy consumption and lower photocatalytic efficiency reside on the low TiO_2 activation under in visible spectra. However, under UV light (300 W), there is a significant increase of the photocatalytic efficiency, up to 90%, underlining the significance of matching the electronic structure of each component With the radiation source. Based on the potential difference of CB and VB in TiO_2 and $LaNiO_3$, they can form excellent S-scheme heterojunction.

The photocatalytic activity of type II heterostructure ($UiO-66/CdIn_2S_4$ [101]), p-n heterostructures ($SnO_2@ZnS$ [102]) and Schottky heterojunction ($Ag/BiVO_4/rGO$ [103]) Was tested in 10 mg/L TCS solution. The optimum energy consumption corresponds to $UiO-66/CdIn_2S_4$, able to reach 92% photocatalytic efficiency after 180 min of irradiation With 150 W Vis light source. The $UiO-66/CdIn_2S_4$ type II heterostructure uses the combined advantages of better charge carrier's channelization, high resistance to charge recombination (due to the favourable band alignment) and high specific 3D microflower-like morphology. Using $Ag/BiVO_4/rGO$ heterostructure obtained by a hydrothermal process, the TCS Was completely removed after 120 min of irradiation With 300 W Vis light source. The high photocatalytic activity of $Ag/BiVO_4/rGO$ is the result of the three-way synergy mechanism, in Which the photogenerated electrons from the CB of $BiVO_4$ Will benefit from the graphene transfer channels and the enhanced migration through Schottky $Ag/BiVO_4$ barrier. $SnO_2@ZnS$ heterostructure With sheets morphology containing cubic ZnS and tetragonal SnO_2 crystalline structures is able to attempt 40% photocatalytic efficiency after 120 min of irradiation With 500 W Vis light source. In this case, the energy consumption is higher due to interactions between TCS and photocatalyst surface. It Was found that hydrated PhACs molecules are preferably adsorbed on the SnO_2 surface rather than on the ZnS surface, Which decreases the number of active sites.

The photocatalytic properties of $Bi_7O_9I_3/Bi_5O_7I$ [104] heterostructure Were investigated using a 500 W Vis light source and 20 mg/L TCS aqueous solution. $Bi_7O_9I_3/Bi_5O_7I$ heterostructure With bone-stick-like morphology Was obtained by in situ thermal treatment and exhibited 89.28% photocatalytic efficiency after 180 min of irradiation. The heterostructure contains two n-type semiconductors, Where the photogenerated electrons are transferred from the CB of $Bi_7O_9I_3$ to the CB of Bi_5O_7I and can be trapped by the molecular oxygen to form superoxidative radicals. The influence of the light spectra on the photocatalytic removal of highly concentrated TCS (50 mg/L) solution Was studied on $p-ZnIn_2S_4/rGO/n-g-C_3N_4$ [105] heterostructure. The irradiation Was done With a 20 W UV source and 2 W Vis source for 120 min. $ZnIn_2S_4/rGO/g-C_3N_4$ heterostructure With sheet-like morphology Was obtained by hydrothermal process and exhibited similar photocatalytic efficiencies in UV (100%) and Vis (97%) radiation. It Was concluded that it is possible to have ten times lower energy consumption using the same heterostructure, by optimizing the light spectra and intensity accordingly With the semiconductor components. The ternary system follows a Z-scheme charges

transport, Where the rGO accelerate the electron transfer and the band energy difference between g-C_3N_4 and $ZnIn_2S_4$ prolongs the charge lifetime and promotes electron-hole separation.

Three Z-scheme heterostructures (Ag/AgCl/$BiVO_4$ [106], Ag/AgBr/$ZnFe_2O_4$ [107] and g-C_3N_4/TiO_2 [108]) Were employed to investigate CBZ (10 mg/L) photocatalytic removal under Vis light. Ag/AgCl/$BiVO_4$ and Ag/AgBr/$ZnFe_2O_4$ Were obtained by ultrasonication, and the photocatalytic experiments Were done using similar parameters (93.38 W Vis light source and 240 min irradiation period). Three times more CBZ Was removed using the same energy consumption by Ag/AgCl/$BiVO_4$ heterostructure (70.6%), compared With Ag/AgBr/$ZnFe_2O_4$. The photocatalytic activity difference Was attributed to the band energy positions, Which are more close in Ag/AgCl/$BiVO_4$ (-0.16 eV CB AgCl/0.33 eV CB $BiVO_4$) heterostructure than that of Ag/AgBr/$ZnFe_2O_4$ (0.1 eV AgBr/-1.5 eV $ZnFe_2O_4$) heterostructure resulting in shorter transition time and lower recombination rate. g-C_3N_4/TiO_2 heterostructure With sheets-like morphology obtained by calcination method shows better photocatalytic efficiency (99.77%), using lower radiation intensity (50 W) for a longer period (360 min). The high photocatalytic activity is attributed to g-C_3N_4, Which has a high specific area and can enlarge the light absorbance spectra.

The SA photocatalytic removal in the presence of 300 W light source Was studied using two WO_3-based heterostructures obtained by one-pot (TiO_2/WO_3 [81]) and hydrothermal (WO_3/Bi_2WO_6 [109]) processes. WO_3/Bi_2WO_6 heterostructure With flower-like morphology Was tested using 5 mg/L SA solution and Vis light source. After 360 min of irradiation, the WO_3/Bi_2WO_6 heterostructure following a Z-scheme mechanism has reached 74.5% photocatalytic efficiency, due to the dramatic increases of visible light absorption induced by (1 1 0) facet of WO_3. In this case, the active sites of the photocatalyst have been transferred from (0 1 0) facet of Bi_2WO_6 to (1 1 0) facet of WO_3. The TiO_2/WO_3 heterostructure mechanism Was previously presented in relation to MG dye. The photocatalytic evaluation Was done under UV irradiation for 60 min, and the photocatalytic efficiency Was 42%. The photocatalytic efficiency Was correlated With the ten times higher SA concentration (50 mg/L) and five times shorter irradiation period. Compared With WO_3/Bi_2WO_6, the TiO_2/WO_3 heterostructure has optimized energy consumption in correlation With the photocatalytic experimental conditions.

TiO_2-NT's@Ag-HA heterostructure [110] obtained by photoreduction Was used to evaluate the influence of visible (100 W) and full spectrum (120 W) light on the photocatalytic activity toward 28 mg/L SA solution. As expected, due to the TiO_2 content, after 240 min of irradiation, the photocatalytic efficiency under full spectrum (75%) Was significantly higher than that under Vis spectrum (30%). The superior photocatalytic efficiency Was attributed to the combined effect of a local surface plasmon resonance, induced by silver nanoparticles and the formation of additional levels in TiO_2 band gap due to Ti^{3+} oxidation state at nanotubes surface. $Bi_{12}TiO_{20}$/g-C_3N_4 heterostructure [64] previously presented in relation to RhB dye Was also tested for SA (10 mg/L) removal, in similar photocatalytic conditions (500 W Vis light source, 50 min irradiation period). However, the photocatalytic efficiency is considerably lower (50%) for SA compared With RhB (97%) due to the smaller SA adsorption on the heterostructure surface.

The removal of IBF (10 mg/L) Was investigated using 60 W (Co_3O_4/BiOI [111]), 300 W ($W_{18}O_{49}$/g-C_3N_4 [112]) and 500 W (Fe_3O_4@MIL-53(Fe) [113]) Vis light sources intensities. Plates-like Co_3O_4/BiOI heterostructure obtained by solvothermal process exhibits 93.87% photocatalytic efficiency after 60 min of irradiation. The Co_3O_4/BiOI Z-scheme mechanism benefits from the improved separation of the photoexcited charge carriers, induced by the built-in electric field formed between the BiOI microspheres and the Co_3O_4 Wormy epitaxy. In the presence of 300 W radiation source and 60 min irradiation period, the $W_{18}O_{49}$/g-C_3N_4 With sheets-like morphology exhibits 96.3% photocatalytic efficiency. Compared With Co_3O_4/BiOI, the photocatalytic efficiency improvement Was moderate, considering that the radiation intensity Was significantly higher. The same heterostructure Was tested under NIR irradiation for 120 min, and the results indicate low photocatalytic efficiency (39.2%) due to the limited absorbance range. However, this value is promising, considering that

most of the photocatalytic materials exhibit neither or very low photocatalytic activity under NIR irradiation. $W_{18}O_{49}$/g-C_3N_4 heterostructure follows a Z-scheme mechanism Where the oxygen vacancies in $W_{18}O_{49}$ can lead to LSPR effect and induce the formation of hot electrons, Which can significantly improve the amount of effective photogenerated electrons and provide unique hot electrons injection. Fe_3O_4@MIL-53(Fe) heterostructure With polyhedron particles morphology Was obtained by calcinations, and the photocatalytic investigations Were done using a 500 W Vis light source. The IBF Was completely removed after 60 min irradiation period, due to high MIL-53(Fe) Vis absorbance induced by the spin-allowed d transition Fe^{3+} on Fe–O cluster. The energy consumption is higher compared With the previously presented studies. The calcination process Was also used to produce Bi_2O_3-TiO_2/carbon [114] heterostructure With S-scheme charges transport. The photocatalytic activity Was evaluated using 20 mg/L IBF solution and 120 min irradiation With 300 W Vis light source. Bi_2O_3-TiO_2/carbon heterostructure Was able to completely remove the IBF due to the synergic role of Bi_2O_3 and TiO_2 on photogenerated electrons and the tuneable charge carrier's mobility through carbon channels.

High (100 mg/L) and low (2 mg/L) IBF concentrations Were used to evaluate the photocatalytic activity of CdS–SnS–SnS_2/rGO [115] and g-C_3N_4/TiO_2/Fe_3O_4@SiO_2 [116] heterostructures. CdS–SnS–SnS_2/rGO containing hexagonal CdS, SnS_2, and orthorhombic SnS Was obtained by solvothermal process and exhibits sheets-like morphology. After 60 min of irradiation With 300 W visible light source, the photocatalytic efficiency achieved Was 84.4%. The energy consumption is reasonable considering that the IBF concentration Was 100 mg/L. CdS–SnS–SnS_2/rGO benefits from a double heterojunction Where rGO Works as a mediator transfer for photogenerated electrons from CB of SnS to CB of SnS_2 and finally to the CB of CdS. The lower IBF concentration (2 mg/L) Was used to evaluate g-C_3N_4/TiO_2/Fe_3O_4@SiO_2 photocatalytic performance, during 15 min of irradiation With 64 W Vis source. g-C_3N_4/TiO_2/Fe_3O_4@SiO_2 heterostructure With sheets-like morphology Was obtained by sol–gel method. The photocatalytic efficiency Was 97%, and the energy consumption fits the photocatalytic parameters. Compared With CdS–SnS–SnS_2/rGO photocatalytic parameters, the g-C_3N_4/TiO_2/Fe_3O_4@SiO_2 heterostructure uses not only 50 times lower IBF concentration but also 4.7 lower light intensity and 4 times shorter irradiation to exhibit good photocatalytic efficiency.

A 5 mg/L SMZ solution Was employed to evaluate the photocatalytic activity of g-C_3N_4/TNTs [117] sheets-like and Pd-Bi_2MoO_6/g-C_3N_4 [118] flake-like heterostructures both following Z-scheme mechanisms. Pd–Bi_2MoO_6/g-C_3N_4 heterostructure is characterized by low energy consumption, being able to achieve 98.8% photocatalytic efficiency after 90 min of irradiation With 36 W Vis light source. In this heterostructure, Pd act as an electron mediator facilitating the charge migration. g-C_3N_4/TNTs heterostructure is able to induce total SMZ removal at high energy consumption, using a 450 W Vis source for 300 min irradiation period. The high photocatalytic efficiency is attributed to in situ transformations of titanate to anatase and rutile, leading to the formation of nanoscale "hot spots" and then subsequent charge transfer as Well as to the large specific surface of TNTs skeleton. At higher SMZ (40 mg/L) concentration, the $CuFe_2O_4$/Ti_3C_2 [119] heterostructure With sheets-like morphology exhibits 70% photocatalytic efficiency after 60 min of irradiation With 300 W Vis light source. $CuFe_2O_4$/Ti_3C_2 follows a Z-scheme charges transport in Which the Ti_3C_2 flakes serve as a shuttle and trap location for light-induced electrons.

Table 2. Recent representative studies on heterostructures photocatalytic application for pharmaceutical active compounds removal.

Heterostructure Composition	Synthesis Method	Morphology/Crystallinity	Pollutant and Concentration (mg/L)	Radiation Type, Intensity (*I*), Irradiation Time (*t*)	Efficiency and Rate Constant (min⁻¹)	Ref.
BN/B-doped-g-C_3N_4	In situ growth	Sheet/hexagonal BN	TC = 10	Vis I = 300 W t = 60 min	88.1%/ 0.034	[91]
WO_3/g-C_3N_4	Polymerization	Sheet/crystalline WO_3-g-C_3N_4	TC = 10	Vis I = 300 W t = 180 min	97%/ np *	[79]

Table 2. *Cont.*

Heterostructure Composition	Synthesis Method	Morphology/Crystallinity	Pollutant and Concentration (mg/L)	Radiation Type, Intensity (*I*), Irradiation Time (*t*)	Efficiency and Rate Constant (min^{-1})	Ref.
$Ag_3PO_4/Co_3(PO_4)_2/g\text{-}C_3N_4$	Precipitation	3D flower/crystalline $Co_3(PO_4)_2$, g-C_3N_4 and Ag_3PO_4	TC = 10	Vis I = 300 W t = 120 min	88%/ 0.0159	[93]
g-C_3N_4-decorated ZrO_{2-x}	Anodic oxidation and PVD	Tube/tetragonal and monoclinic zirconia	TC = 10	Vis I = 300 W t = 60 min	90.6%/ 0.0474	[92]
$ZnIn_2S_4/BiPO_4$	Hydrothermal	Flower/monoclinic $BiPO_4$	TC = 40	Vis I = 300 W t = 90 min	84%/ 0.0201	[98]
$AgI/Bi_2MoO_6/AgBi(MoO_4)_2$	Hydrothermal	Sheets/crystalline AgI, Bi_2MoO_6 and $AgBi(MoO_4)_2$	TC = 5	Vis I = 400 W t = 90 min	91.9%/ 0.0097	[99]
$MoS_2/g\text{-}C_3N_4/Bi_{24}O_{31}Cl_{10}$	Calcination	Sheet/monoclinic $Bi_{24}O_{31}Cl_{10}$ and MoS_2	TC = 20	Vis I = 300 W t = 50 min	97.5%/ 0.0642	[94]
$CuBi_2O_4/Bi_2WO_6$	Hydrothermal	Pseudo-sphere/tetragonal $CuBi_2O_4$ and orthorhombic Bi_2WO_6	TC = 20	Vis I = 300 W t = 120 min	93%/ 0.0286	[95]
$La(OH)_3/BiOCl$	Microwave	Sheet/crystalline BiOCl	TC = 20	Vis I = 5 W t = 60 min	85%/ 0.037	[96]
$WS_2/BiOBr$	Hydrothermal	Plates/tetragonal BiOBr	TC = 20 CIP = 20	Vis I = 500 W t = 100 min	96% (TC) 92% (CIP)/ np (TC) 0.01708 (CIP)	[68]
$BiOCl/CQDs/rGO$	Hydrothermal	Sheet/tetragonal BiOCl	CIP = 20	Vis I = 300 W t = 100 min	87%/ 0.0146	[97]
$LaNiO_3/TiO_2$	In situ sol–gel	Granular/anatase TiO_2 and perovskite $LaNiO_3$	CIP = 10	UV, Vis $I_{UV, Vis}$ = 300 W t = 180 min	90% (UV) 55% (Vis)/ np	[77]
PVPbiochar@$ZnF_2O_4/BiOBr$	Solvothermal	Sheet/tetragonal BiOBr, spinel $ZnFe_2O_4$	CIP = 15	Vis I = 300 W t = 60 min	84%/ np	[100]
$UiO\text{-}66/CdIn_2S_4$	Solvothermal	3D flower/pristine CIS	TCS = 10	Vis I = 150 W t = 180 min	92%/ 0.0094	[101]
$Ag/BiVO_4/rGO$	Hydrothermal	Irregular Particles/monoclinic $BiVO_4$	TCS = 10	Vis I = 300 W t = 120 min	100%/ np	[103]
$SnO_2@ZnS$	Hydrothermal	Sheet/cubic ZnS, tetragonal SnO_2	TCS = 10	Vis I = 500 W t = 120 min	40%/ 0.0033	[102]
$Bi_7O_9I_3/Bi_5O_7I$	Calcination	Bone-stick/crystalline $Bi_7O_9I_3$ and Bi_5O_7I	TCS = 20	Vis I = 500 W t = 180 min	89.28%/ 0.0168	[104]
p-$ZnIn_2S_4/rGO/n$-g-C_3N_4	Hydrothermal	Sheet/crystalline $ZnIn_2S_4$	TCS = 50	UV, Vis I_{UV} = 20 W I_{Vis} = 2 W t = 120 min	100% (UV) 97% (Vis)/ np	[105]
$Ag/AgCl/BiVO_4$	Ultrasonication	Octahedral particle/monoclinic BiVO4, crystalline AgCl and Ag	CBZ = 10	Vis I = 93.38 W t = 240 min	70.6%/ np	[106]
g-C_3N_4/TiO_2	Calcination	Sheet/crystalline g-C_3N_4, anatase TiO_2	CBZ = 10	Vis I = 50 W t = 360 min	99.77%/ 0.1796	[108]
$Ag/AgBr/ZnFe_2O_4$	Ultrasonication	Spherical/cubic AgBr and $ZnFe_2O_4$	CBZ = 10	Vis I = 93.38 W t = 240 min	22.7%/ np	[107]
$Bi_{12}TiO_{20}/g\text{-}C_3N_4$	Ultrasonication	Spherical/cubic $Bi_{12}TiO_{20}$	SA = 10	Vis I = 500 W t = 50 min	50%/ np	[64]
WO_3/Bi_2WO_6	Hydrothermal	Flower/orthorhombic Bi_2WO_6	SA = 5	Vis I = 300 W t = 360 min	74.5%/ 0.00435	[109]

Table 2. *Cont.*

Heterostructure Composition	Synthesis Method	Morphology/Crystallinity	Pollutant and Concentration (mg/L)	Radiation Type, Intensity (I), Irradiation Time (t)	Efficiency and Rate Constant (min^{-1})	Ref.
TiO$_2$-NT's@Ag-HA	Photoreduction	Tubes/anatase TiO$_2$	SA = 28	Full Spectrum (FS), Vis I_{FS} = 120 W I_{Vis} = 100 W t = 240 min	75% (FS) 30% (Vis)/ 0.00581 (FS) 0.00129 (Vis)	[110]
TiO$_2$/WO$_3$	One pot	Hollow sphere/anatase TiO$_2$ and monoclinic WO$_3$	SA = 50	UV I = 300 W t = 60 min	42%/ np	[81]
CdS-SnS-SnS$_2$/rGO	Solvothermal	Sheet/hexagonal CdS, SnS$_2$ and orthorhombic SnS	IBF = 100	Vis I = 300 W t = 60 min	84.4%/ 0.0257	[115]
Bi$_2$O$_3$-TiO$_2$/carbon	Calcination	Particle/anatase and rutile TiO$_2$	IBF = 20	Vis I = 300 W t = 120 min	100%/ 0.0290	[114]
W$_{18}$O$_{49}$/g-C$_3$N$_4$	Hydrothermal	Sheet/monoclinic W$_{18}$O$_{49}$	IBF = 10	Vis, NIR $I_{Vis, NIR}$ = 300 W t_{Vis} = 60 min t_{NIR} = 120 min	96.3% (Vis) 39.2% (NIR)/0.0464 (Vis) 0.0027 (NIR)	[112]
Fe$_3$O$_4$@MIL-53(Fe)	Calcination	Particles with polyhedron structure/crystalline Fe$_3$O$_4$	IBF = 10	Vis I = 500 W t = 60 min	99%/ 0.0471	[113]
Co$_3$O$_4$/BiOI	Solvothermal	Plates/crystalline Co$_3$O$_4$, Tetragonal BiOI	IBF = 10	Vis I = 60 W t = 60 min	93.87%/ 0.0945	[111]
g-C$_3$N$_4$/TiO$_2$/Fe$_3$O$_4$@SiO$_2$	Sol–gel	Sheet/standard magnetite, anatase TiO$_2$	IBF = 2	Vis I = 64 W t = 15 min	97%/ np	[116]
g-C$_3$N$_4$/TNTs	Hydrothermal	Sheet/anatase and rutile TiO$_2$	SMZ = 5	Vis I = 450 W t = 300 min	100%/ 0.0193	[117]
Pd-Bi$_2$MoO$_6$/g-C$_3$N$_4$	Precipitation	Flake/crystalline Bi$_2$MoO$_6$ and g-C$_3$N$_4$	SMZ = 5	Vis I = 36 W t = 90 min	98.8%/ 0.0440	[118]
CuFe$_2$O$_4$/Ti$_3$C$_2$	Hydrothermal	Sheet/spinel CuFe$_2$O$_4$	SMZ = 40	Vis I = 300 W t = 60 min	70%/ 0.0128	[119]

* not provided.

To sum up, the most energy-efficient photocatalytic systems for PhACs removal correspond to Z-scheme ZnIn$_2$S$_4$/rGO/C$_3$N$_4$ heterostructure using 4 Wh to remove 48.5 mg/L of TCS and type II La(OH)$_3$/BiOCl heterostructures requiring 5 Wh to remove 17 mg/L of TC. Higher energy consumption is attributed to p-n SnO$_2$@ZnS heterostructures, Which use 1000 Wh to remove 4.0 mg/L of TC.

4. Conclusions

The diversification of pollutant type and concentration in Wastewater has underlined the importance of finding new alternatives to traditional treatment methods. AOPs, among others, are considered as a promising candidate to efficiently remove organic pollutants such as dyes of PhACs. The present minireview has considered several process parameters (radiation spectra, light intensity and irradiation period) and materials properties (crystallinity, morphology or charge transportation mechanism). However, there are also other parameters that Were not the subject of this investigation but can have an important influence on the photocatalytic efficiency (specific surface, catalyst dosage, irradiance, pollutant type, etc.).

The presence of compatible crystalline structures between the heterostructure partners is a prerequisite to assure a good interfacial junction, Which allows a facile charge carriers transport. The flower-like and sheets morphologies seem to host a larger number of active surface sites and, consequently, a higher photocatalytic activity. In order to obtain a balance between the energy consumption and photocatalytic efficiency, it is important to optimize the light spectra and intensity

as Well as the irradiance period according to the heterostructure type, pollutant molecule and concentrations. The total pollutant removal With the expense of high energy consumption Will raise questions about the process sustainability and future large-scale implementation. It is possible to remove 85% of TC (20 mg/L) With low energy consumption (5 W Vis source, 60 min of irradiation) as Well as 97.5% With higher energy consumption (300 W Vis, 50 min of irradiation). Sustainability is a key parameter to be considered When designing environmental treatment processes. AOPs based on photoactive heterostructures require chemically stable materials for long Working periods and low energy consumption.

Dyes removal using photocatalytic heterostructures Was evaluated for different molecules, and most of the results indicate high efficiencies. However, PhACs removal by photocatalytic processes still requires more experimental investigation on various molecules in order to have a detailed evaluation of the degradation mechanisms, including the by-products formation. The presence of by-products after the photocatalytic degradation of dyes and PhACs represents an important issue due to the hazard risk induced by their toxicity and environmental persistence. Consequently, the degradation mechanism of each pollutant molecule must be studied in relation to the photocatalytic parameters. The transfer from the laboratory investigations to large-scale applications Will outline significant challenges in terms of economic costs and sustainability.

As perspectives, it Will be recommended to use a uniform standardization regarding the photocatalytic activity experimental investigations. The scientific articles give several and often noncompatible parameters, Which make the comparative investigation more difficult. For example, regarding the radiation parameters, most papers refer to light intensity (W), and other provides the irradiance (mW/cm^2), Which is more accurate. The photocatalytic efficiency improvement With few percentages is made by significant increase of the energy consumption instead of improving the intrinsic materials properties. Coupling photocatalysis With other techniques (adsorption, biodegradation, etc.) can be another pathway to follow for optimum energy consumption and organic pollutant removal.

References

1. Cheng, D.; Ngo, H.H.; Wei, D. A critical review on antibiotics and hormones in swine Wastewater: Water pollution problems and control approaches. *J. Hazard. Mater.* **2020**, *387*, 121682. [CrossRef] [PubMed]
2. Gautam, K.; Anbumani, S. Ecotoxicological effects of organic micro-pollutants on the environment. In *Current Developments in Biotechnology and Bioengineering*, 1st ed.; Varjani, S., Pandey, A., Tyagi, R.D., Ngo, H.H., Larroche, C., Eds.; Elsevier: New York, NY, USA, 2020; pp. 481–501.
3. Duarte, R.M.; Matos, J.T.; Senesi, N. Organic pollutants in soils. In *Soil Pollutions*, 1st ed.; Duarte, A.C., Cachada, A., Rocha-Santos, T., Eds.; Elsevier: New York, NY, USA, 2018; pp. 103–126.
4. Wood, D.; Shaw, S.; Cawte, T.; Shanen, E.; Heyst, B.V. An overview of photocatalyst immobilization methods for air pollution remedation. *Chem. Eng. J.* **2020**, *391*, 123490. [CrossRef]
5. Hader, D.P.; Banaszak, A.T.; Helbling, E.W. Anthropogenic pollution of aquatic ecosystems: Emerging problems With global implications. *Sci. Total Environ.* **2020**, *713*, 136586. [CrossRef] [PubMed]
6. Libralato, G.; Lofrano, G.; Siciliano, A.; Gambino, E.; Boccia, G.; Federica, C.; Francesco, A.; Galdiero, E.; Gesuele, R.; Guida, M. Toxicity assessment of Wastewater after advanced oxidation processes for emerging contaminants' degradation. In *Visible Light Active Structured Photocatalysts for the Removal of Emerging Contaminants*, 1st ed.; Sacco, O., Vaiano, V., Eds.; Elsevier: New York, NY, USA, 2020; pp. 195–211.

7.　Kaplan, A.; Mamane, H.; Lester, Y.; Avisar, D. Trace organic compound removal from Wastewater reverse-osmosis concentrate by advanced oxidation processes With UV/O_3/H_2O_2. *Materials* **2020**, *13*, 2785. [CrossRef] [PubMed]

8.　Cui, M.; Zeng, L.; Qin, W.; Feng, J. Measures for reducing nitrate leaching in orchards: A review. *Environ. Pollut.* **2020**, *263*, 114553. [CrossRef]

9.　Serban, I.; Enesca, A. Metal Oxides-Based Semiconductors for Biosensors Applications. *Front. Chem.* **2020**, *8*, 354. [CrossRef]

10.　Tahreen, A.; Jami, M.S.; Ali, F. Role of electrocoagulation in Wastewater treatment: A developmental review. *J. Water Proc. Eng.* **2020**, *37*, 101440. [CrossRef]

11.　Guo, W.; Umar, A.; Du, Y.; Wang, L.; Pei, M. Surface Modification of Bentonite With Polymer Brushes and Its Application as an Efficient Adsorbent for the Removal of Hazardous Dye Orange I. *Nanomaterials* **2020**, *10*, 1112. [CrossRef]

12.　Enesca, A.; Andronic, L.; Duta, A. The influence of surfactants on the crystalline structure, electrical and photocatalytic properties of hybrid multi-structured (SnO_2, TiO_2 and WO_3) thin films. *Appl. Surf. Sci.* **2012**, *258*, 4339–4346. [CrossRef]

13.　Cornejo, O.M.; Murrieta, M.F.; Castañeda, L.F.; Nava, J.L. Characterization of the reaction environment in flow reactors fitted With BDD electrodes for use in electrochemical advanced oxidation processes: A critical review. *Electrochim. Acta* **2020**, *33120*, 135373. [CrossRef]

14.　Malakootian, M.; Shahesmaeili, A.; Faraji, M.; Amiri, H.; Martinez, S.S. Advanced oxidation processes for the removal of organophosphorus pesticides in aqueous matrices: A systematic review and meta-analysis. *Process Saf. Environ.* **2020**, *134*, 292–307. [CrossRef]

15.　Han, M.; Duan, X.; Cao, G.; Zhuc, S.; Ho, S.H. Graphitic nitride-catalyzed advanced oxidation processes (AOPs) for landfill leachate treatment: A mini review. *Process Saf. Environ.* **2020**, *139*, 230–240. [CrossRef]

16.　Yang, L.; He, L.; Xue, J.; Ma, Y.; Zhang, Z. UV/$SO_3{}^{2-}$ based advanced reduction processes of aqueous contaminants: Current status and prospects. *Chem. Eng. J.* **2020**, *3971*, 125412. [CrossRef]

17.　Bresolin, B.M.; Park, Y.; Bahnemann, D.W. Recent Progresses on Metal Halide Perovskite-Based Material as Potential Photocatalyst. *Catalysts* **2020**, *10*, 709. [CrossRef]

18.　Chen, L.; Tang, J.; Song, L.N.; Chen, P.; Yin, S.F. Heterogeneous photocatalysis for selective oxidation of alcohols and hydrocarbons. *Appl. Catal. B* **2019**, *242*, 379–388. [CrossRef]

19.　Chauhan, D.K.; Jain, S.; Battula, V.R.; Kailasam, K. Organic motif's functionalization via covalent linkage in carbon nitride: An exemplification in photocatalysis. *Carbon* **2019**, *152*, 40–58. [CrossRef]

20.　Hu, X.; Ma, Q.; Wang, X.; Yang, Y.; Liu, N.; Zhang, C.; Kawazoe, N.; Chen, G.; Yang, Y. Layered Ag/Ag_2O/$BiPO_4$/Bi_2WO_6 heterostructures by two-step method for enhanced photocatalysis. *J. Catal.* **2020**, *387*, 28–38. [CrossRef]

21.　Ojha, D.P.; Karki, H.P.; Song, J.H.; Kim, H.J. Amine-assisted synthesis of $FeWO_4$ nanorodg-C_3N_4 for enhanced visible light-driven Z-scheme photocatalysis. *Compos. Part B Eng.* **2019**, *1601*, 277–284. [CrossRef]

22.　Wetchakun, K.; Wetchakun, N.; Sakulsermsuk, S. An overview of solar/visible light-driven heterogeneous photocatalysis for Water purification: TiO_2- and ZnO-based photocatalysts used in suspension photoreactors. *J. Ind. Eng. Chem.* **2019**, *7125*, 19–49. [CrossRef]

23.　Yao, S.; Wang, J.; Zhou, X.; Zhou, S.; Pu, X.; Li, W. One-pot low-temperature synthesis of BiOX/TiO_2 hierarchic composites of adsorption coupled With photocatalysis for quick degradation of colored and colorless organic pollutants. *Adv. Powder Technol.* **2020**, *31*, 1924–1932. [CrossRef]

24.　Kant, S.; Pathania, D.; Singh, P.; Dhiman, P.; Kumar, A. Removal of malachite green and methylene blue by $Fe_{0.01}Ni_{0.01}Zn_{0.98}O$/polyacrylamide nanocompositeusing coupled adsorption and photocatalysis. *Appl. Catal. B* **2014**, *147*, 340–352. [CrossRef]

25.　Ma, Y.; Xiong, H.; Zhao, Z.; Yu, Y.; Zhou, D.; Dong, S. Model-based evaluation of tetracycline hydrochloride removal and mineralization in an intimately coupled photocatalysis and biodegradation reactor. *Chem. Eng. J.* **2018**, *351*, 967–975. [CrossRef]

26.　Li, F.; Lan, X.; Wang, L.; Kong, X.; Xu, P.; Tai, Y.; Liu, G.; Shi, J. An efficient photocatalyst coating strategy for intimately coupled photocatalysis and biodegradation (ICPB): Powder spraying method. *Chem. Eng. J.* **2020**, *383*, 123092. [CrossRef]

27. Ceretta, M.B.; Vieira, Y.; Wolski, E.A.; Foletto, E.L.; Silvestri, S. Biological degradation coupled to photocatalysis by ZnO/polypyrrole composite for the treatment of real textile Wastewater. *J. Water Proc. Eng.* **2020**, *35*, 101230. [CrossRef]

28. Grcic, I.; Vrsaljko, D.; Katancic, Z.; Papic, S. Purification of household grey Water loaded With hair colorants by solar photocatalysis using TiO_2-coated textile fibers coupled flocculation With chitosan. *J. Water Proc. Eng.* **2015**, *5*, 15–27. [CrossRef]

29. Xu, T.; Wang, P.; Wang, D.; Zhao, K.; Wei, M.; Liu, X.; Liu, H.; Cao, J.; Fan, H.; Yang, L. Ultrasound-assisted synthesis of hyper-dispersed type-II tubular $Fe_3O_4@SiO_2@ZnO/ZnS$ core/shell heterostructure for improved visible-light photocatalysis. *J. Alloy. Compd.* **2020**, *838*, 155689. [CrossRef]

30. Wang, H.; Li, J.; Quan, X.; Wu, Y. Enhanced generation of oxidative species and phenol degradation in a discharge plasma system coupled With TiO_2 photocatalysis. *Appl. Catal. B* **2008**, *83*, 72–77. [CrossRef]

31. Liu, J.; Wang, Y.; Ma, J.; Peng, Y.; Wang, A. A review on bidirectional analogies between the photocatalysis and antibacterial properties of ZnO. *J. Alloy. Compd.* **2019**, *78330*, 898–918. [CrossRef]

32. Li, H.; Zhang, N.; Zhao, F.; Liu, T.; Wang, Y. Facile Fabrication of a Novel Au/Phosphorus-Doped g-C_3N_4 Photocatalyst With Excellent Visible Light Photocatalytic Activity. *Catalysts* **2020**, *10*, 701. [CrossRef]

33. Enesca, A.; Yamaguchi, Y.; Terashima, C.; Fujishima, A.; Nakata, K.; Duta, A. Enhanced UV-Vis photocatalytic performance of the $CuInS_2/TiO_2/SnO_2$ hetero-structure for air decontamination. *J. Catal.* **2017**, *350*, 174–181. [CrossRef]

34. Roques-Carmes, T.; Alem, H.; Hamieh, T.; Toufaily, J.; Frochot, C.; Villieras, F. Different strategies of surface modification to improve the photocatalysis properties: Pollutant adsorption, visible activation, and catalyst recovery. In *Handbook of Smart Photocatalytic Materials*, 1st ed.; Hussain, C.M., Mishra, A.K., Eds.; Elsevier: New York, NY, USA, 2020; pp. 39–57.

35. Zhang, X.; Teng, S.Y.; Loy, A.C.M.; How, B.S.; Leong, W.D.; Tao, X. Transition Metal Dichalcogenides for the Application of Pollution Reduction: A Review. *Nanomaterials* **2020**, *10*, 1012. [CrossRef] [PubMed]

36. Mouchaal, Y.; Enesca, A.; Mihoreanu, C.; Khelil, A.; Duta, A. Tuning the opto-electrical properties of SnO_2 thin films by Ag^{+1} and In^{+3} co-doping. *Mater. Sci. Eng. B* **2015**, *199*, 22–29. [CrossRef]

37. Song, B.; Zeng, Z.; Zeng, G.; Gong, J.; Tang, X. Powerful combination of g-C_3N_4 and LDHs for enhanced photocatalytic performance: A review of strategy, synthesis, and applications. *Adv. Colloid Interface Sci.* **2019**, *272*, 101999. [CrossRef] [PubMed]

38. Salgado, B.C.; Cardeal, R.A.; Valentini, A. Photocatalysis and Photodegradation of Pollutants. In *Nanomaterials Applications for Environmental Matrices*, 1st ed.; Nascimento, R.F., Ferreira, O.P., De Paula, A.J., Neto, V.O., Eds.; Elsevier: New York, NY, USA, 2019; pp. 449–488.

39. Enesca, A.; Andronic, L.; Duta, A. Optimization of Opto-Electrical and Photocatalytic Properties of SnO_2 Thin Films Using Zn^{2+} and W^{6+} Dopant Ions. *Catal. Lett.* **2012**, *142*, 224–230. [CrossRef]

40. Yang, Y.; Zhou, C.; Xiong, W.; Zeng, G.; Huang, D.; Zhang, C.; Wang, W.; Song, B.; Tang, X.; Li, X.; et al. Recent advances in application of graphitic carbon nitride-based catalysts for degrading organic contaminants in Water through advanced oxidation processes beyond photocatalysis: A critical review. *Water Res.* **2020**, *184*, 116200. [CrossRef] [PubMed]

41. Ren, Y.; Wang, C.; Qi, Y.; Chen, Z.; Xu, Q. CO_2-Induced Defect Engineering: A New Protocol by Doping Vacancies in 2D Heterostructures for Enhanced Visible-Light Photocatalysis. *Appl. Surf. Sci.* **2017**, *419*, 573–579. [CrossRef]

42. Pedanekar, R.S.; Shaikh, S.K.; Rajpure, K.Y. Thin film photocatalysis for environmental remediation: A status review. *Curr. Appl. Phys.* **2020**, *20*, 931–952. [CrossRef]

43. He, W.; Sun, Y.; Jiang, G.; Li, Y.; Dong, F. Defective Bi_4MoO_9/Bi metal core/shell heterostructure: Enhanced visible light photocatalysis and reaction mechanism. *Appl. Catal. B* **2018**, *239*, 619–627. [CrossRef]

44. Xia, Y.; Wang, J.; Xu, L.; Li, X.; Huang, S. A room-temperature methane sensor based on Pd-decorated ZnO/rGO hybrids enhanced by visible light photocatalysis. *Sens. Actuat. B* **2020**, *3041*, 127334. [CrossRef]

45. Andronic, L.; Enesca, A.; Cazan, C.; Visa, M. TiO_2-active carbon composites for Wastewater photocatalysis. *J. Sol-Gel Sci. Technol.* **2014**, *71*, 399–405. [CrossRef]

46. Irani, E.; Amoli-Diva, M. Hybrid adsorption–photocatalysis properties of quaternary magneto-plasmonic ZnO/MWCNTs nanocomposite for applying synergistic photocatalytic removal and membrane filtration in industrial Wastewater treatment. *J. Photochem. Photobiol. A Chem.* **2020**, *39115*, 112359. [CrossRef]

47. Kusmierek, E. Semiconductor Electrode Materials Applied in Photoelectrocatalytic Wastewater Treatment—An Overview. *Catalysts* **2020**, *10*, 439. [CrossRef]

48. Xiao, W.Z.; Xu, L.; Rong, Q.Y.; Dai, X.Y.; Wang, L.L. Two-dimensional H-TiO$_2$/MoS$_2$(WS$_2$) van der Waals heterostructures for visible-light photocatalysis and energy conversion. *Appl. Surf. Sci.* **2020**, *504*, 144425. [CrossRef]

49. Kanakkillam, S.S.; Krishnan, B.; Avellaneda, D.A.; Shaji, S. Surfactant free stable cobalt oxide nanocolloid in Water by pulsed laser fragmentation and its thin films for visible light photocatalysis. *Colloid. Surface. A* **2020**, *5945*, 124657. [CrossRef]

50. Rafiq, U.; Majid, K. Mitigating the charge recombination by the targeted synthesis of Ag$_2$WO$_4$/Bi$_2$Fe$_4$O$_9$ composite: The facile union of orthorhombic semiconductors towards efficient photocatalysis. *J. Alloy. Compd.* **2020**, *84225*, 155876. [CrossRef]

51. Jia, S.; Xu, M.; Chen, S.; Yan, J.; Ma, X. A hierarchical sandwich-structured MoS$_2$/SnO$_2$/CC heterostructure for high photocatalysis performance. *Mater. Lett.* **2019**, *236*, 697–701. [CrossRef]

52. Li, D.; Song, H.; Meng, X.; Shen, T.; Sun, J.; Han, W.; Wang, X. Effects of Particle Size on the Structure and Photocatalytic Performance by Alkali-Treated TiO$_2$. *Nanomaterials* **2020**, *10*, 546. [CrossRef]

53. Estahbanati, M.R.K.; Feilizadeh, M.; Babin, A.; Mei, B.; Iliuta, M.C. Selective photocatalytic oxidation of cyclohexanol to cyclohexanone: A spectroscopic and kinetic study. *Chem. Eng. J.* **2020**, *38215*, 122732. [CrossRef]

54. Guo, X.; Zhou, X.; Li, X.; Shao, C.; Liu, Y. Bismuth oxychloride (BiOCl)/copper phthalocyanine (CuTNPc) heterostructures immobilized on electrospun polyacrylonitrile nanofibers With enhanced activity for floating photocatalysis. *J. Colloid Interface Sci.* **2018**, *525*, 187–195. [CrossRef]

55. Li, X.; Chen, D.; Li, N.; Xu, Q.; Lu, J. Efficient reduction of Cr(VI) by a BMO/Bi$_2$S$_3$ heterojunction via synergistic adsorption and photocatalysis under visible light. *J. Hazard. Mater.* **2020**, *4005*, 123243. [CrossRef]

56. Mintcheva, N.; Gicheva, G.; Panayotova, M.; Kulinich, S.A. Room-Temperature Synthesis of ZnS Nanoparticles Using Zinc Xanthates as Molecular Precursors. *Materials* **2020**, *13*, 171. [CrossRef] [PubMed]

57. Li, Y.; Cai, C.; Gu, Y.; Cheng, W.; Zhao, C. Novel electronic properties of a new MoS$_2$/TiO$_2$ heterostructure and potential applications in solar cells and photocatalysis. *Appl. Surf. Sci.* **2017**, *414*, 34–40. [CrossRef]

58. González-Burciaga, L.A.; Núñez-Núñez, C.M.; Morones-Esquivel, M.M.; Avila-Santos, M.; Lemus-Santana, A.; Proal-Nájera, J.B. Characterization and Comparative Performance of TiO$_2$ Photocatalysts on 6-Mercaptopurine Degradation by Solar Heterogeneous Photocatalysis. *Catalysts* **2020**, *10*, 118. [CrossRef]

59. Liu, N.; Lu, N.; Yu, H.T.; Chen, S.; Quan, X. Efficient day-night photocatalysis performance of 2D/2D Ti$_3$C$_2$/Porous g-C$_3$N$_4$ nanolayers composite and its application in the degradation of organic pollutants. *Chemosphere* **2020**, *246*, 125760. [CrossRef] [PubMed]

60. Hu, X.; Wang, G.; Wang, J.; Hu, Z.; Su, Y. Step-scheme NiO/BiOI heterojunction photocatalyst for rhodamine photodegradation. *App. Surf. Sci.* **2020**, *511*, 145499. [CrossRef]

61. Kumar, R.S.; Min, K.S.; Lee, S.H.; Mergu, N.; Son, Y.A. Synthesis of novel panchromatic porphyrin-squaraine dye and application towards TiO$_2$ combined photocatalysis. *J. Photochem. Photobiol. A* **2020**, *397*, 112595. [CrossRef]

62. Tsai, C.G.; Tseng, W.J. Preparation of TiN–TiO$_2$ composite nanoparticles for organic dye adsorption and photocatalysis. *Ceram. Int.* **2020**, *46*, 14529–14535. [CrossRef]

63. Hernández-Carrillo, M.A.; Torres-Ricárdez, R.; García-Mendoza, M.F.; Ramírez-Morales, E.; Pérez-Hernández, G. Eu-modified ZnO nanoparticles for applications in photocatalysis. *Catal. Today* **2020**, *3491*, 191–197. [CrossRef]

64. Cao, L.; Li, Y.F.; Tong, Y.; Yang, R.; Sun, L.; Cao, O.; Chen, R. A novel Bi$_{12}$TiO$_{20}$/g-C$_3$N$_4$ hybrid catalyst With a bionic granum configuration for enhanced photocatalytic degradation of organic pollutants. *J. Hazard. Mater.* **2019**, *379*, 120808. [CrossRef]

65. Shende, A.G.; Tiwari, C.S.; Bhoyar, T.H.; Vidyasagar, D.; Umare, S.S. BWO nano-octahedron coupled With layered g-C$_3$N$_4$: An efficient visible light active photocatalyst for degradation of cationic/anionic dyes, and N$_2$ reduction. *J. Molec. Liq.* **2019**, *296*, 111771. [CrossRef]

66. Zhang, Y.; Xu, J.; Mei, J.; Sarina, S.; Wu, Z.; Liao, T.; Yan, C.; Sun, Z. Strongly interfacial-coupled 2D-2D TiO$_2$/g-C$_3$N$_4$ heterostructure for enhanced visible-light induced synthesis and conversion. *J. Hazard. Mater.* **2020**, *394*, 122529. [CrossRef] [PubMed]

67. Zhong, Q.; Lan, H.; Zhang, M.; Zhu, H.; Bu, M. Preparation of heterostructure g-C₃N₄/ZnO nanorods for high photocatalytic activity on different pollutants (MB, RhB, Cr(VI) and eosin). *Ceram. Int.* **2020**, *46*, 12192–12199. [CrossRef]

68. Fu, S.; Yuan, W.; Liu, X.; Yan, Y.; Liu, H.; Li, L.; Zhao, F.; Zhou, J. A novel 0D/2D WS₂/BiOBr heterostructure With rich oxygen vacancies for enhanced broad-spectrum photocatalytic performance. *J. Colloid. Interf. Sci.* **2020**, *569*, 150–163. [CrossRef]

69. Wang, Y.; Wang, Q.; Zhang, H.; Wu, Y.; Jia, Y.; Jin, R.; Gao, S. CTAB-assisted solvothermal construction of hierarchical Bi₂MoO₆/Bi₅O₇Br With improved photocatalytic performances. *Sep. Purif. Technol.* **2020**, *242*, 116775. [CrossRef]

70. Zhao, K.; Zhang, Z.; Feng, Y.; Lin, S.; Li, H.; Gao, X. Surface oxygen vacancy modified Bi₂MoO₆/MIL-88B(Fe) heterostructure With enhanced spatial charge separation at the bulk & interface. *Appl. Catal. B* **2020**, *268*, 118740.

71. Bao, L.; Yang, F.; Cheng, D.; Pan, X.; Zhang, H.; Zhao, F.; Zhao, S.; Tegus, O. Modified electronic structure of Ta₂O₅ via surface decorated With Ta₃B₂ nanodots for enhanced photocatalytic activity. *App. Surf. Sci.* **2020**, *513*, 145767. [CrossRef]

72. Jin, J.; Xie, Y. Ultraviolet light induced oxygen vacancy-rich BiPO₄₋ₓ/Bi₂S₃ nanorods With enhanced photocatalytic activity and mechanism. *Res. Chem. Intermed.* **2019**, *45*, 5609–5623. [CrossRef]

73. Mandal, B.; Panda, J.; Paul, P.K.; Sarkar, R.; Tudu, B. MnFe₂O₄ decorated reduced graphene oxide heterostructures: Nanophotocatalyst for methylene blue dye degradation. *Vacuum* **2020**, *173*, 109150. [CrossRef]

74. Alido, J.P.M.; Sari, F.N.I.; Ting, Y.M. Synthesis of Ag/hybridized 1T-2H MoS₂/TiO₂ heterostructure for enhanced visible-light photocatalytic activity. *Ceram. Int.* **2019**, *45*, 23651–23657. [CrossRef]

75. Tian, Q.; Fang, G.; Ding, L.; Ran, M.; Zhang, H.; Pan, A.; Shen, K.; Deng, Y. ZnAl₂O₄/Bi₂MoO₆ heterostructures With enhanced photocatalytic activity for the treatment of organic pollutants and eucalyptus chemimechanical pulp Wastewater. *Mater. Chem. Phys.* **2020**, *241*, 122299. [CrossRef]

76. Çinar, B.; Kerimoglu, I.; Tonbül, B.; Demirbüken, A.; Dursun, S.; Kaya, I.C.; Kalem, V.; Akyildiz, H. Hydrothermal/electrospinning synthesis of CuO plate-like particles/TiO₂ fibers heterostructures for high-efficiency photocatalytic degradation of organic dyes and phenolic pollutants. *Mater. Sci. Semic. Proces.* **2020**, *109*, 104919. [CrossRef]

77. Chen, C.; Zhou, J.; Geng, J.; Bao, R.; Wang, Z.; Xia, J.; Li, H. Perovskite LaNiO₃/TiO₂ step-scheme heterojunction With enhanced photocatalytic activity. *Appl. Surf. Sci.* **2020**, *503*, 144287. [CrossRef]

78. Zhou, J.; Zhang, Z.; Kong, X.; He, F.; Zhao, R.; Wua, R.; Wei, T.; Wang, L.; Feng, J. A novel P-N heterojunction With staggered energy level based on ZnFe₂O₄ decorating SnS₂ nanosheet for efficient photocatalytic degradation. *App. Surf. Sci.* **2020**, *510*, 145442. [CrossRef]

79. Yan, H.; Zhu, Z.; Long, Y.; Li, W. Single-source-precursor-assisted synthesis of porous WO₃/g-C₃N₄ With enhanced photocatalytic property. *Colloid. Surfaces A* **2019**, *582*, 123857. [CrossRef]

80. Neto, N.F.A.; Lima, A.B.; Bomio, M.R.D.; Motta, F.V. Microwave-assisted hydrothermal synthesis of Ag₂Mo₁₋ₓWₓO₄ (x = 0, 0.25, 0.50, 0.75 and 1 mol%) heterostructures for enhanced photocatalytic degradation of organic dyes. *J. Alloy. Compd.* **2020**, *844*, 156007.

81. Wei, Y.; Huang, Y.; Fang, Y.; Zhao, Y.; Luo, D.; Guo, Q.; Fan, L.; Wu, J. Hollow mesoporous TiO₂/WO₃ sphere heterojunction With high visiblelight-driven photocatalytic activity. *Mater. Res. Bull.* **2019**, *119*, 110571. [CrossRef]

82. Zhou, Q.; Li, L.; Xin, A.; Yu, Y.; Wang, L.; Zhang, W. Visible light response and heterostructure of composite CdS@ZnSeZnO to enhance its photocatalytic activity. *J. Alloys Compd.* **2020**, *813*, 152190. [CrossRef]

83. Yulizar, Y.; Apriandanua, D.O.B.; Ashna, R.I. La2CuO4-decorated ZnO nanoparticles With improved photocatalytic activity for malachite green degradation. *Chem. Phys. Lett.* **2020**, *755*, 137749. [CrossRef]

84. Jia, J.; Du, X.; Zhang, Q.; Liu, E.; Fan, J. Z-scheme MgFe₂O₄/Bi₂MoO₆ heterojunction photocatalyst With enhanced visible light photocatalytic activity for malachite green removal. *Appl. Surf. Sci.* **2019**, *492*, 527–539. [CrossRef]

85. Isari, A.A.; Hayati, F.; Kakavandi, B.; Rostami, M.; Dehghanifard, E. Cu co-doped TiO₂@functionalized SWCNT photocatalyst coupled With ultrasound and visible-light: An effective sono-photocatalysis process for pharmaceutical Wastewaters treatment. *Chem. Eng. J.* **2020**, *392*, 123685. [CrossRef]

86. Pan, Y.; Liu, X.; Zhang, W.; Liu, Z.; Chen, M. Advances in photocatalysis based on fullerene C60 and its derivatives: Properties, mechanism, synthesis, and applications. *Appl. Catal. B* **2020**, *26515*, 118579. [CrossRef]

87. Ahmad, K.; Ghatak, H.R.; Ahuja, S.M. A review on photocatalytic remediation of environmental pollutants and H_2 production through Water splitting: A sustainable approach. *Environ. Technol. Innov.* **2020**, *19*, 100893. [CrossRef]

88. Kovacic, M.; Papac, J.; Kusic, H.; Karamanis, P.; Bozic, A.L. Degradation of polar and non-polar pharmaceutical pollutants in Water by solar assisted photocatalysis using hydrothermal TiO_2-SnS_2. *Chem. Eng. J.* **2020**, *382*, 122826. [CrossRef]

89. Zhang, X.; Yuan, X.; Jiang, L.; Zhang, J.; Zeng, G. Powerful combination of 2D g-C_3N_4 and 2D nanomaterials for photocatalysis: Recent advances. *Chem. Eng. J.* **2020**, *39015*, 124475. [CrossRef]

90. Gopinath, K.P.; Madhav, N.V.; Krishnan, A.; Malolan, R.; Rangarajan, G. Present applications of titanium dioxide for the photocatalytic removal of pollutants from Water: A review. *J. Environ. Manag.* **2020**, *27015*, 110906. [CrossRef]

91. Acharya, L.; Nayak, S.; Pattnaik, S.P.; Acharya, R.; Parida, K. Resurrection of boron nitride in p-n type-II boron nitride/B-doped-g-C_3N_4 nanocomposite during solid-state Z-scheme charge transfer path for the degradation of tetracycline hydrochloride. *J. Colloid Interface Sci.* **2020**, *566*, 211–223. [CrossRef]

92. Chen, Q.; Yang, W.; Zhu, J.; Fu, L.; Li, D.; Zhou, L. Enhanced visible light photocatalytic activity of g-C_3N_4 decorated ZrO_{2-x} nanotubes heterostructure for degradation of tetracycline hydrochloride. *J. Hazard. Mater.* **2020**, *384*, 121275. [CrossRef]

93. Shi, W.; Liu, C.; Li, M.; Lin, X.; Guo, F.; Shi, J. Fabrication of ternary Ag_3PO_4/$Co_3(PO_4)_2$/g-C_3N_4 heterostructure With following Type II and Z-Scheme dual pathways for enhanced visible-light photocatalytic activity. *J. Hazard. Mater.* **2020**, *389*, 121907. [CrossRef]

94. Kang, J.; Jin, C.; Li, Z.; Wang, M.; Chen, Z.; Wang, Y. Dual Z-scheme MoS_2/g-C_3N_4/$Bi_{24}O_{31}Cl_{10}$ ternary heterojunction photocatalysts for enhanced visible-light photodegradation of antibiotic. *J. Alloys Compd.* **2020**, *825*, 153975. [CrossRef]

95. Wang, L.; Yang, G.; Wang, D.; Lu, C.; Guan, W.; Li, Y.; Deng, J.; Crittenden, J. Fabrication of the flower-flake-like $CuBi_2O_4$/Bi_2WO_6 heterostructure as efficient visible-light driven photocatalysts: Performance, kinetics and mechanism insight. *Appl. Surf. Sci.* **2019**, *495*, 143521. [CrossRef]

96. Zhou, Z.; Xu, H.; Li, D.; Zou, Z.; Xia, Z. Microwave-assisted synthesis of La(OH)$_3$/BiOCl n-n heterojunctions With high oxygen vacancies and its enhanced photocatalytic properties. *Chem. Phys. Lett.* **2019**, *736*, 136805. [CrossRef]

97. Huang, J.; Chen, W.; Yu, X.; Fu, X.; Zhu, Y.; Zhang, Y. Fabrication of a ternary BiOCl/CQDs/rGO photocatalyst: The roles of CQDs and rGO in adsorption-photocatalytic removal of ciprofloxacin. *Colloid. Surf. A* **2020**, *597*, 124758. [CrossRef]

98. Lu, C.; Guo, F.; Yan, Q.; Zhang, Z.; Li, D.; Wang, L.; Zhou, Y. Hydrothermal synthesis of type II $ZnIn_2S_4$/$BiPO_4$ heterojunction photocatalyst With dandelion-like microflower structure for enhanced photocatalytic degradation of tetracycline under simulated solar light. *J. Alloys Compd.* **2019**, *811*, 151976. [CrossRef]

99. Zhou, T.; Zhang, H.; Ma, X.; Zhang, X.; Zhu, Y.; Zhang, A.; Cao, Y.; Yang, P. Construction of AgI/Bi_2MoO_6/AgBi(MoO$_4$)$_2$ multi-heterostructure composite nanosheets for visible-light photocatalysis. *Mater. Today Commun.* **2020**, *23*, 100903. [CrossRef]

100. Chen, M.; Dai, Y.; Guo, J.; Yang, H.; Liu, D.; Zhai, Y. Solvothermal synthesis of biochar@$ZnFe_2O_4$/BiOBr Z-scheme heterojunction for efficient photocatalytic ciprofloxacin degradation under visible light. *Appl. Surf. Sci.* **2019**, *493*, 1361–1367. [CrossRef]

101. Bariki, R.; Majhi, D.; Das, K.; Behera, A.; Mishra, B.G. Facile synthesis and photocatalytic efficacy of UiO-66/$CdIn_2S_4$ nanocomposites With flowerlike 3D-microspheres towards aqueous phase decontamination of triclosan and H_2 evolution. *Appl. Catal. B* **2020**, *270*, 118882. [CrossRef]

102. Hojamberdiev, M.; Czech, B.; Goktaş, A.C.; Yubuta, K.; Kadirova, Z.C. SnO_2@ZnS photocatalyst With enhanced photocatalytic activity for the degradation of selected pharmaceuticals and personal care products in model Wastewater. *J. Alloy. Compd.* **2020**, *827*, 154339. [CrossRef]

103. Li, M.; Xu, G.; Guan, Z.; Wang, Y.; Yu, H.; Yu, Y. Synthesis of Ag/$BiVO_4$/rGO composite With enhanced photocatalytic degradation of triclosan. *Sci. Total Environ.* **2019**, *664*, 230–239. [CrossRef]

104. Chang, C.; Yang, H.; Mu, W.; Cai, Y.; Wang, L.; Yang, L.; Qin, H. In situ fabrication of bismuth oxyiodide ($Bi_7O_9I_3$/Bi_5O_7I) n-n heterojunction for enhanced degradation of triclosan (TCS) under simulated solar light irradiation. *Appl. Catal. B.* **2019**, *254*, 647–658. [CrossRef]

105. Yu, T.; Wu, W.W.; Liu, L.; Gao, C.; Yang, T. Novel ternary p-$ZnIn_2S_4$/rGO/n-g-C_3N_4 Z-scheme nanocatalyst With enhanced antibiotic degradation in a dark self-biased fuel cell. *Ceram. Int.* **2020**, *46*, 9567–9574. [CrossRef]

106. Yentür, G.; Dükkanci, M. Synthesis of Visible-Light Heterostructured Photocatalyst of Ag/AgCl Deposited on (040) Facet of Monoclinic $BiVO_4$ for Efficient Carbamazepine Photocatalytic Removal. *Appl. Surf. Sci.* **2020**, in press. [CrossRef]

107. Yentür, G.; Dükkancı, M. Fabrication of magnetically separable plasmonic composite photocatalyst of Ag/AgBr/$ZnFe_2O_4$ for visible light photocatalytic oxidation of carbamazepine. *Appl. Surf. Sci.* **2020**, *510*, 145374. [CrossRef]

108. Hu, Z.; Cai, X.; Wang, Z.; Li, S.; Wang, Z.; Xie, X. Construction of carbon-doped supramolecule-based g-C_3N_4/TiO_2 composites for removal of diclofenac and carbamazepine: A comparative study of operating parameters, mechanisms, degradation pathways. *J. Hazard. Mater.* **2019**, *380*, 120812. [CrossRef] [PubMed]

109. Chen, X.; Li, Y.; Li, L. Facet-engineered surface and interface design of WO_3/Bi_2WO_6 photocatalyst With direct Z-scheme heterojunction for efficient salicylic acid removal. *Appl. Surf. Sci.* **2020**, *508*, 144796. [CrossRef]

110. Plodinec, M.; Grcic, I.; Willinger, M.G.; Hammud, A.; Huang, X.; Panzic, I.; Gajovi, A. Black TiO_2 nanotube arrays decorated With Ag nanoparticles for enhanced visible-light photocatalytic oxidation of salicylic acid. *J. Alloy. Compd.* **2019**, *776*, 883–896. [CrossRef]

111. Malefane, M.E.; Feleni, U.; Mafa, P.J.; Kuvarega, A.T. Fabrication of direct Z-scheme Co_3O_4/BiOI for ibuprofen and trimethoprim degradation under visible light irradiation. *Appl. Surf. Sci.* **2020**, *514*, 145940. [CrossRef]

112. Deng, Y.; Feng, C.; Tang, L.; Zhou, Y.; Chen, Z.; Feng, H.; Wang, J.; Yu, J.; Liu, Y. Ultrathin low dimensional heterostructure composites With superior photocatalytic activity: Insight into the multichannel charge transfer mechanism. *Chem. Eng. J.* **2020**, *393*, 124718. [CrossRef]

113. Liu, N.; Wang, J.; Wu, J.; Li, Z.; Huang, W.; Zheng, Y.; Lei, J.; Zhang, X.; Tang, L. Magnetic Fe_3O_4@MIL-53(Fe) nanocomposites derived from MIL-53(Fe) for the photocatalytic degradation of ibuprofen under visible light irradiation. *Mater. Res. Bull.* **2020**, *132*, 111000. [CrossRef]

114. Wang, N.; Li, X.; Yang, Y.; Zhou, Z.; Shang, Y.; Zhuang, X.; Zhang, T. Two-stage calcination composite of Bi_2O_3-TiO_2 supported on powdered activated carbon for enhanced degradation of sulfamethazine under solar irradiation. *J. Water Proc. Eng.* **2020**, *35*, 101220. [CrossRef]

115. Liang, M.; Yu, Y.; Wang, Y.; Yu, Y. Remarkably efficient charge transfer through a double heterojunction mechanism by a CdS-SnS-SnS_2/rGO composite With excellent photocatalytic performance under visible light. *J. Hazard. Mater.* **2020**, *391*, 121016. [CrossRef]

116. Kumar, A.; Khan, M.; Zeng, X.; Lo, I. Development of g-C_3N_4/TiO_2/Fe_3O_4@SiO_2 heterojunction via sol-gel route: A magnetically recyclable direct contact Z-scheme nanophotocatalyst for enhanced photocatalytic removal of ibuprofen from real sewage effluent under visible light. *Chem. Eng. J.* **2018**, *353*, 645–656. [CrossRef]

117. Ji, H.; Du, P.; Zhao, D.; Li, S.; Sun, F.; Duin, E.C.; Liu, W. 2D/1D graphitic carbon nitride/titanate nanotubes heterostructure for efficient photocatalysis of sulfamethazine under solar light: Catalytic "hot spots" at the rutile–anatase–titanate interfaces. *Appl. Catal. B* **2020**, *263*, 118357. [CrossRef]

118. Di, G.; Zhu, Z.; Zhang, H.; Qiu, Y.; Yin, D.; Crittenden, J. Simultaneous sulfamethazine oxidation and bromate reduction by Pd mediated Z-scheme Bi_2MoO_6/g-C_3N_4 photocatalysts: Synergetic mechanism and degradative pathway. *Chem. Eng. J.* **2020**, *401*, 126061. [CrossRef]

119. Cao, Y.; Fang, Y.; Lei, X.; Tan, B.; Hu, X.; Liu, B.; Chen, Q. Fabrication of novel $CuFe_2O_4$/MXene hierarchical heterostructures for enhanced photocatalytic degradation of sulfonamides under visible light. *J. Hazard. Mater.* **2020**, *387*, 122021. [CrossRef] [PubMed]